Cell Reports

Article

Postmitotic Hoxa5 Expression Specifies Pontine Neuron Positional Identity and Input Connectivity of Cortical Afferent Subsets

Graphical Abstract

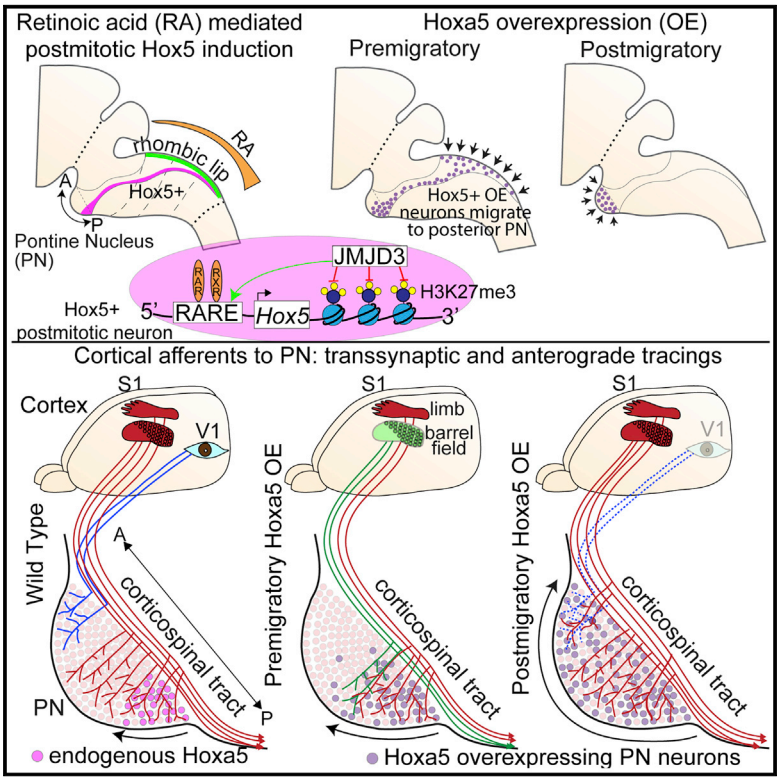

Highlights

- Expression of Hox5 factors is induced in postmitotic pontine nucleus (PN) neurons
- Hoxa5 expression drives neurons to settle posteriorly in PN
- Hoxa5-dependent identity determines pre-synaptic input regardless of neuron position
- Hoxa5-expressing neurons avoid visual and prefer somatosensory cortical afferents

Authors

Upasana Maheshwari, Dominik Kraus, Nathalie Vilain, ..., Thomas Di Meglio, Sebastien Ducret, Filippo M. Rijli

Correspondence

filippo.rijli@fmi.ch

In Brief

Maheshwari et al. show that Hox5 transcription factors are induced in postmitotic pontine nucleus (PN) neurons. The Hoxa5-dependent intrinsic program regulates topographic migration and determines specificity of pre-synaptic cortical inputs regardless of PN neuron position. Hoxa5+ PN neurons avoid visual and prefer somatosensory cortical afferents revealing cortico-pontine sub-circuit molecular logic.

Maheshwari et al., 2020, Cell Reports *31*, 107767
June 16, 2020
https://doi.org/10.1016/j.celrep.2020.107767

CellPress

Cell Reports

CellPress
OPEN ACCESS

Article

Postmitotic Hoxa5 Expression Specifies Pontine Neuron Positional Identity and Input Connectivity of Cortical Afferent Subsets

Upasana Maheshwari,[1,2,7] Dominik Kraus,[1,2,7] Nathalie Vilain,[1] Sjoerd J.B. Holwerda,[1,4] Vanja Cankovic,[1] Nicola A. Maiorano,[1] Hubertus Kohler,[1] Daisuke Satoh,[1,3] Markus Sigrist,[1,3] Silvia Arber,[1,3] Claudius F. Kratochwil,[1,5] Thomas Di Meglio,[1,6] Sebastien Ducret,[1] and Filippo M. Rijli[1,2,8,*]

[1]Friedrich Miescher Institute for Biomedical Research, Maulbeerstrasse 66, 4058 Basel, Switzerland
[2]University of Basel, 4051 Basel, Switzerland
[3]Biozentrum, University of Basel, Kingelbergstrasse 70, 4056 Basel, Switzerland
[4]Present address: Novartis Institutes for Biomedical Research, Novartis Pharma AG, Basel, Switzerland
[5]Present address: Department of Biology, University of Konstanz, Konstanz, Germany
[6]Present address: Universidad Autónoma de Madrid, Centro de Biología Molecular, Cabrera 1, 28049 Madrid, Spain
[7]These authors contributed equally
[8]Lead Contact
*Correspondence: filippo.rijli@fmi.ch
https://doi.org/10.1016/j.celrep.2020.107767

SUMMARY

The mammalian precerebellar pontine nucleus (PN) has a main role in relaying cortical information to the cerebellum. The molecular determinants establishing ordered connectivity patterns between cortical afferents and precerebellar neurons are largely unknown. We show that expression of Hox5 transcription factors is induced in specific subsets of postmitotic PN neurons at migration onset. *Hox5* induction is achieved by response to retinoic acid signaling, resulting in Jmjd3-dependent derepression of Polycomb chromatin and 3D conformational changes. Hoxa5 drives neurons to settle posteriorly in the PN, where they are monosynaptically targeted by cortical neuron subsets mainly carrying limb somatosensation. Furthermore, *Hoxa5* postmigratory ectopic expression in PN neurons is sufficient to attract cortical somatosensory inputs regardless of position and avoid visual afferents. Transcriptome analysis further suggests that Hoxa5 is involved in circuit formation. Thus, *Hoxa5* coordinates postmitotic specification, migration, settling position, and subcircuit assembly of PN neuron subsets in the cortico-cerebellar pathway.

INTRODUCTION

Neural circuit assembly sequentially involves neuronal fate specification, migration, and establishment of precise input-output axonal wiring and synaptic connectivity. Coordination among these processes is critical, especially when distant brain structures need to be topographically connected; yet molecular determinants able to coordinate these processes remain largely unknown.

The cerebral cortex and cerebellum are two major structures involved in sensorimotor coordination through extensive reciprocal connections (D'Angelo and Casali, 2013). Cerebro-cerebellar projections are mainly relayed through the mossy fiber projection neurons of the precerebellar pontine nucleus (PN) (Allen and Tsukahara, 1974). In mice, PN neurons are generated in the caudal hindbrain between embryonic day (E)12.5 and E16.5 from the dorsal rhombomere (r)6- to r8-derived *Wnt1*$^{+}$/*Atoh1*$^{+}$ progenitors of the lower rhombic lip (lRL) (Harkmark, 1954; Pierce, 1973; Tan and Le Douarin, 1991; Rodriguez and Dymecki, 2000; Wang et al., 2005; Farago et al., 2006; Di Meglio et al., 2013). From the lRL, PN neurons undergo a long-distance tangential migration, forming the anterior extramural stream (AES), and settle in the rostral pons on both sides of the ventral midline (Altman and Bayer, 1987; Rodriguez and Dymecki, 2000).

Members of the Hox transcription factor family play important roles during hindbrain neuronal and circuit development (Philippidou and Dasen, 2013; Oury et al., 2006; Di Bonito et al., 2013; Bechara et al., 2015; Karmakar et al., 2017). In the precerebellar system, *Hox* expression molecularly defines specific subsets of rhombic lip progenitors and neurons migrating in the AES and settling in distinct rostrocaudal positions of the PN (Di Meglio et al., 2013). In particular, Hox paralog group 5 (*Hox5*) expression defines neuron subsets migrating in ventral AES and settling in the posterior PN; in dorsal AES, the *Unc5b* guidance receptor maintains positioning of *Hox5*-negative PN neurons that settle anteriorly in the PN, whereas *Unc5b* is downregulated in ventral AES by Hox5 factors (Di Meglio et al., 2013).

In the corticopontine pathway, axons from primary somatosensory cortex (S1), primary visual cortex (V1), or primary motor cortex (M1) mostly target centroposterior, anterolateral, or medial and rostral areas of the PN, respectively, roughly preserving cortical area topographic organization (Wiesendanger and Wiesendanger, 1982; Mihailoff et al., 1984; O'Leary and Terashima, 1988;

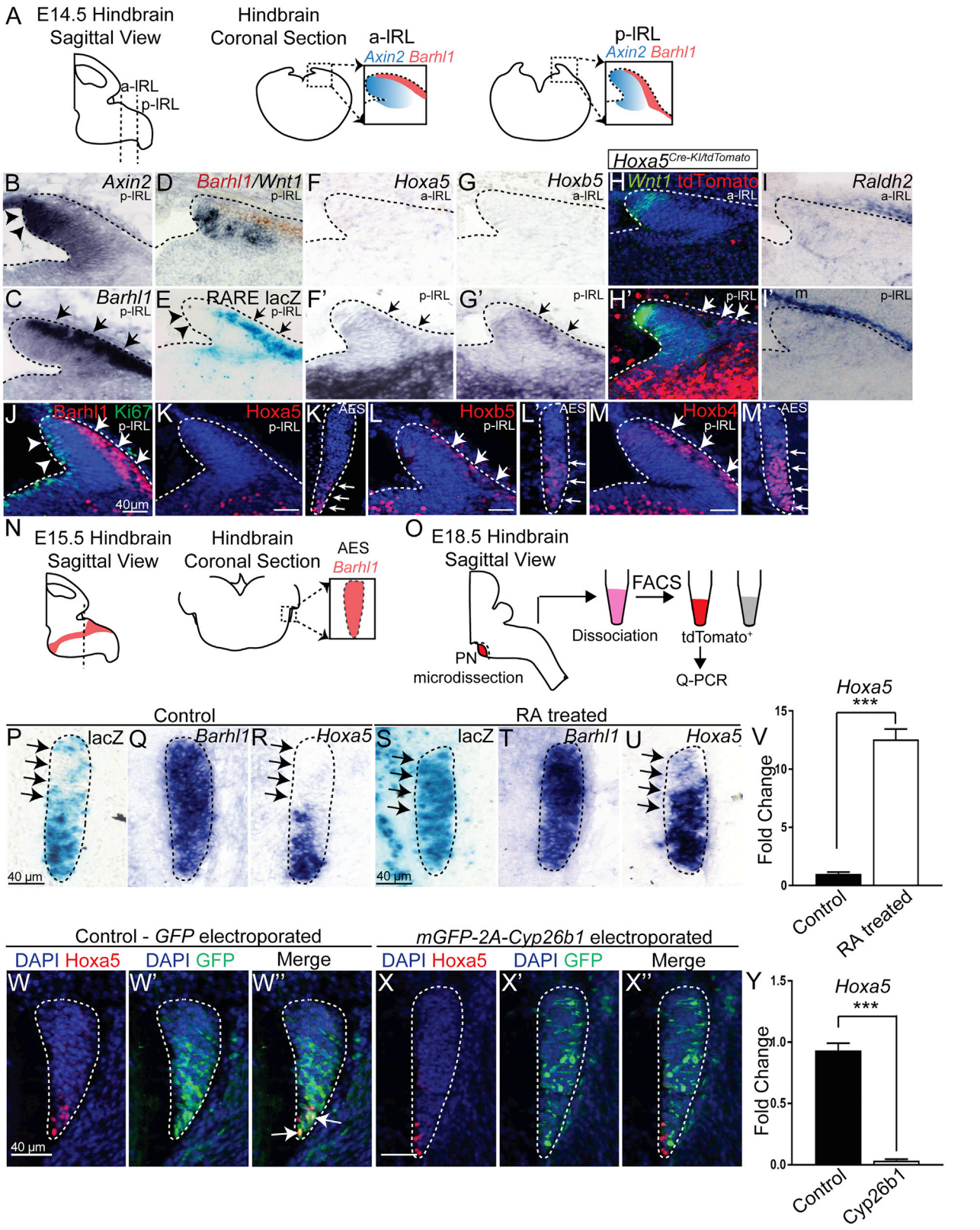

(legend on next page)

Leergaard et al., 2000b; Leergaard and Bjaalie, 2007). At the cellular level, an internal-external lamellar organization of cortical axon terminal fields might topographically match an inside-out organization of PN neurons based on their birthdate (Altman and Bayer, 1987; Leergaard et al., 1995). Moreover, an intrinsic positional organization of PN neurons according to their rostro-caudal origin in the IRL is topographically maintained during AES migration and PN assembly (Di Meglio et al., 2013). However, the molecular basis of corticopontine connectivity is still poorly understood.

Here, we found that expression of Hox5 transcription factors is induced in subsets of postmitotic PN neurons from migration onset. Spatially restricted *Hox5* gene induction requires local response to retinoic acid (RA) signaling from the meninges, resulting in Jmjd3-dependent derepression of Polycomb chromatin and higher order chromatin conformational changes. Moreover, Hoxa5 expression in PN neurons is sufficient to drive them to the posterior PN. By trans-synaptic viral tracings, we show that cortical neurons targeting Hoxa5-expressing neurons in the posterior PN are enriched with limb somatosensory afferents. On the other hand, widespread Hoxa5 expression after neuronal migration is instructive to attract somatosensory and avoid visual cortical inputs, regardless of neuron position in the PN. Lastly, Hoxa5 expression in neuronal subsets regulates transcriptional sub-programs potentially underlying the specificity of their connectivity.

This comprehensive study elucidates how single Hox transcription factors may coordinate precerebellar neuron specification, migration, orderly settling in the PN, and topographic input connectivity from specific cortical neuron subsets. Moreover, these findings further our understanding of the molecular logic underlying sub-circuit assembly and diversification in the mammalian corticopontine pathway.

RESULTS

Hox5 Expression Is Induced Postmitotically in Posterior Subsets of PN Neurons

In the precerebellar system, *Hox2-4* genes are expressed in mitotically active *Wnt1*$^+$ IRL progenitors (Rodriguez and Dymecki, 2000) as well as postmitotic *Barhl1*$^+$ neurons (Figures S1C–S1E; Bulfone et al., 2000; Geisen et al., 2008; Di Meglio et al., 2013). In the E14.5 IRL, *Barhl1* and *Wnt1*, or the Wnt activity marker *Axin2* (Jho et al., 2002), display mutually exclusive expression patterns (Figures 1B–1D), with Ki67$^+$ mitotic cells restricted to the *Wnt1*$^+$/*Barhl1*$^-$ inner IRL portion (Figure 1J). Unlike *Hox2-4* genes, *Hoxa5* and *Hoxb5* were mainly detected in *Barhl1*$^+$/*Ki67*$^-$ postmitotic neurons (Figures 1F′, 1G′, S1F, and S1G). Moreover, *Hoxa5* levels appeared quite low at the onset of migration and more posteriorly induced than *Hoxb5* throughout PN neuron generation from E12.5 to E16.5 (Figures 1F′, 1G′, and S1F–S1I).

To further support these findings, we analyzed the distribution of tdTomato$^+$ cells in *Hoxa5*$^{Cre\text{-}KI/tdTomato}$ (Figures 1H and 1H′; STAR Methods; Table S1) as a proxy for endogenous *Hoxa5*. Consistent with endogenous *Hoxa5* expression, tdTomato$^+$ cells were barely present in the E14.5 *Wnt1*$^+$ mitotic domain, while tdTomato was detected in a few *Wnt1*$^-$ postmitotic neurons of posterior IRL (p-IRL) (Figure 1H′, arrows). Unlike Hoxb5, which was already detected in the *Barhl1*$^+$/*Ki67*$^-$ postmitotic domain of p-IRL (Figures 1K and 1L), accumulation of endogenous Hoxa5 protein was only evident in the AES. In addition, Hoxb4 also appeared to accumulate only in postmitotic neurons (Figure 1M), despite *Hoxb4* expression in both mitotic and postmitotic cells (Figure S1E). Hoxa5$^+$ and Hoxb5$^+$ neurons migrated in ventral AES and settled posteriorly within the developing PN (Figures 1K–1M and S1J–S1M; Di Meglio et al., 2013).

Thus, *Hox5* genes define specific neuron subsets in the posterior PN, with *Hoxa5* specifying the most posterior subset. Moreover, Hox4 and Hox5 transcription factors are only postmitotically expressed, and this may be a specific property of rhombic-lip-derived precerebellar neurons.

Spatially Restricted *Hox5* Expression in Posterior PN Neurons Requires RA Signaling

RA is mainly synthesized by *Raldh2* in the meninges overlaying the IRL (Niederreither and Dollé, 2008; Zhang et al., 2003). At E14.5, we found posterior-high to anterior-low expression of *Raldh2* (Figures 1I and 1I′). Analysis of the *RARE*^{lacZ} reporter mouse line, which provides a readout of endogenous RA response, revealed β-galactosidase (β-gal) staining mostly in

Figure 1. *Hox5* Genes Are Induced in a Subset of IRL-Derived PN Neurons and Require RA Signaling

(A) Drawing illustrating anterior and posterior lower rhombic lip (a-lRL and p-lRL, respectively) at E14.5.

(B–I′) E14.5 wild-type coronal sections showing *in situ* hybridization for *Axin 2* (B), for *Barhl1* (C), and for *Barhl1* (red) and *Wnt1* (blue) (D), labeling postmitotic precerebellar neurons (arrows) and progenitor domain (arrowheads), respectively. (E) *RARE*^{lacz} β-gal-stained coronal section showing strong endogenous retinoid activity in postmitotic posterior IRL (p-IRL; arrows indicate postmitotic neurons, and arrowheads indicate progenitors). *Hoxa5* (F and F′) and *Hoxb5* (G and G′) are expressed in postmitotic neurons of p-IRL (arrows in F′ and G′), not anterior IRL (a-IRL). (H and H′) *Wnt1* (green) and tdTomato (red) immunohistochemistry (IHC) in *Hoxa5*$^{Cre\text{-}KI/tdTomato}$, labeling mitotic domain and *Hoxa5*-driven Cre activity, respectively. The tdTomato signal is only detected in postmitotic neurons in p-IRL (arrows). (I and I′) ISH for *Raldh2* showing lower expression in meninges overlying a-IRL (I) than that in p-IRL (I′).

(J–M′) E14.5 wild-type coronal sections showing IHC for Barhl1 (red) and Ki67 (green) (J), labeling postmitotic neurons and mitotically active progenitors, respectively; Hoxa5 (K and K′), Hoxb5 (L and L′), and Hoxb4 (M and M′) in pIRL (K, L, and M) and in anterior extramural stream (AES) (K′, L′, and M′). Hoxa5 is only detected in AES (arrows in K′), whereas Hoxb5 (L and L′) and Hoxb4 (M and M′) are detected in both postmitotic neurons and AES.

(N and O) Drawings illustrating AES (N) and collection and isolation of PN neurons by FACS for qPCR assay (O).

(P–U) E15.5 untreated *RARE*^{lacz} coronal sections (P–R) or RA treated at E11.5 (S–U), stained with β-gal (P and S) or *in situ* hybridized with *Barhl1* (Q and T) or *Hoxa5* (R and U) (arrows, dorsal AES).

(V) qPCR on FACS-isolated PN neurons from E18.5 control or RA-treated *Atoh1(45)*^{tdTomato} mice (n = 3; $p < 0.0001$).

(W–X″) E15.5 *RARE*^{lacz} coronal sections *in utero* electroporated at E13.5 with *GFP* (W–W″) or *Cyp26b1* (X–X″), showing expression of Hoxa5 (W and X) or GFP (W′ and X′); arrows indicate GFP and Hoxa5 co-expression in W″, not detected in X″.

(Y) qPCR on FACS-isolated neurons from control or *Cyp26b1* electroporated PN (n = 3; $p < 0.001$). Data are presented as mean + SD.

See also Figure S1.

postmitotic IRL-derived neurons (Figures 1E and S1P–S1S), which was ventrodorsally graded in the AES (Figure 1P). *Wnt1*/*Ki67*/β-gal stainings on E12.5–E15.5 *RARE*^{lacZ} serial sections (Figures S1P–S1S) further indicated that the RA response induction is mainly restricted to the postmitotic IRL-derived neurons. Accordingly, β-gal staining and *Hoxb5* transcript distribution overlapped in posterior IRL-derived postmitotic PN neurons (Figures S1N and S1O).

To assess RA dependency of *Hox5* induction, we increased or decreased RA availability *in vivo*. We imaged transverse sections of the E14.5–E15.5 AES, as this allows us to directly visualize on each section the whole contribution of r6- and r8-derived PN neurons dorsoventrally distributed in the AES (Di Meglio et al., 2013) and their RA response (Figure 1N). Exogenous RA administration at E11.5 (STAR Methods) resulted in dorsal expansion of the RA response and *Hoxa5* expression within the *RARE*^{lacZ} AES (Figures 1P–1U). qPCR also confirmed a significant increase in *Hoxa5* expression levels in E18.5 RA-treated *Atoh1(45)*^{tdTomato} PN neurons (Figure 1V; Table S1) dissected and further isolated by fluorescence-activated cell sorting (FACS) (Figure 1O). At this stage, migration is complete (Shinohara et al., 2013), and PNs are prominent and relatively simple structures to dissect.

To assess the effect of decreased RA, we *in utero* electroporated IRL progenitors of *RARE*^{lacZ} embryos at E13.5 with *GFP* or the RA-degrading enzyme *Cyp26b1*. Ectopic induction of *Cyp26b1* resulted in strongly decreased responsiveness to endogenous retinoids (Figures S1T–S1T″). Moreover, *Hoxa5* expression was decreased in electroporated *Cyp26b1*$^{+}$ neurons, as assessed by both Hoxa5 immunohistochemistry (Figures 1W″and 1X″) and *Hoxa5* qPCR in GFP^{+} PN neurons isolated by FACS (Figure 1Y).

In summary, *Hox5* genes are RA targets, and their rostrocaudally restricted expression likely relies on higher endogenous RA activity experienced by posterior versus anterior IRL-derived PN neurons.

Hox5 Transcriptional Induction in Pontine Neurons Requires Jmjd3 Demethylase

Hox5 gene silencing in dorsal AES is maintained by Ezh2 (Di Meglio et al., 2013), a member of Polycomb Repressive Complex 2 (PRC2) which represses chromatin by trimethylation of histone H3 at lysine 27 (H3K27me3) (Margueron and Reinberg, 2011). In E14.5 IRL, *Ezh2* expression was stronger in the mitotic than postmitotic domain and displayed no obvious rostrocaudal bias (Figures S1A and S1A′). Conditional *Ezh2* depletion in *Wnt1*$^{+}$ IRL progenitors (*Wnt1*^{Ezh2cKO}; Table S1) resulted in *Barlh1*$^{+}$ cells partially intermingling with the *Axin2*$^{+}$ domain, which appeared to be reduced (Figures 2A, 2C, 2F, and 2H). Ectopic *Hoxa5* expression was induced, suggesting that *Hox5* gene loci are poised for transcriptional induction throughout the rostrocaudal extent of the IRL (Figures 2B, 2E, 2G, and 2J).

To test whether H3K27me3 depletion is necessary for spatially regulated *Hox5* transcriptional induction, we generated null mutants of the H3K27 demethylase *Kdm6b*/*Jmjd3* (Agger et al., 2007; De Santa et al., 2007; Lan et al., 2007; Lee et al., 2007) (Figures S2A and S2B; STAR Methods). In E14.5 IRL, *Jmjd3* expression pattern was complementary to that of *Ezh2*, with low expression in *Axin2*$^{+}$ and high expression in *Barlh1*$^{+}$ cells, as assessed by β-gal staining in *Jmjd3*$^{+/lacZ}$ mice (Figures S1A and S1B; Table S1). Heterozygous mutant mice were viable and fertile, whereas *Jmjd3*$^{lacZ/lacZ}$ or *Jmjd3*$^{-/-}$ mutant fetuses died perinatally (Burgold et al., 2012). Nonetheless, E18.5 *Jmjd3* homozygous mutant PNs were not grossly affected (Figures S2K and S2L), which allowed for prenatal analysis of *Hox5* gene induction.

In E14.5 *Jmjd3*$^{lacZ/lacZ}$ fetuses, *Hoxa5* was not induced in posterior IRL-derived PN neurons (Figure 2K), whereas the *Axin2* expression domain appeared to be expanded (Figure 2L). Normal *Raldh2* and *Cyp26b1* expression ruled out changes in endogenous RA synthesis or degradation (Figures S2D–S2F and S2H–S2J). *Jmjd3*-dependent regulation was specific to *Hox5* genes, as in *Jmjd3*$^{-/-}$ AES Hoxa5 expression was strongly impaired, whereas Hoxb4 appeared unaffected (Figures 2M–2P). Moreover, qPCR on E18.5 *Atoh1(45)*^{tdTomato};*Jmjd3*$^{-/-}$ FACS-isolated PN neurons showed strong *Hoxa5* reduction, while *Hoxb4* and *Hoxb3* levels were unchanged (Figure 2Q; Figures S2N and S2O).

Lastly, chromatin immunoprecipitation (ChIP) in E14.5 FACS-isolated cells from *Hoxa5*^{tdTomato} mice (Table S1; Figures 2R and 2S) revealed that both the RA receptor (RAR) alpha (RARa) and Jmjd3 bound a previously identified Hoxa5 RA response enhancer (RARE) (Mahony et al., 2011; Figure 2T), indicating that *Hoxa5* is a direct RA transcriptional target.

In summary, *Jmjd3* is involved in alleviating *Ezh2*-dependent chromatin repression at the *Hox5* loci following transcriptional induction by RA and liganded RAR. Integration of local signaling and chromatin remodeling provides an *in vivo* template for spatially restricted, transcription-factor-mediated induction of *Hox5* transcription in a specific subset of pontine neurons.

A 3D Chromatin Switch at *Hox5* Loci Is Induced by *In Vivo* Response to Retinoids

To investigate the role of RA in driving spatially regulated transitions of higher order chromatin conformation at *Hox5* loci in hindbrain neurons, we carried out high-resolution circular chromosome conformation capture followed by high-throughput sequencing (4C-seq) (van de Werken et al., 2012). We collected E14.5 *Hox5*-negative fluorescent cells from *r5-6*^{tdTomato} mice (Table S1), *Hox5*-positive fluorescent cells from *Hoxa5*^{tdTomato} mice, and *Hox*-negative control cells from cerebral cortex (CC) and used *Hoxa5* (Figures 3A–3C and S3C) and *Hoxb5* (Figures S3D–S3G) promoters as viewpoints. In CC, both *Hoxa* and *Hoxb* clusters were organized into a single association domain (Figures S3C and S3D), correlating with their transcriptionally silent state in this tissue. In contrast, in rostrocaudally adjacent *Hox5*-negative and *Hox5*-positive hindbrain neuronal cell populations, *Hoxa5* or *Hoxb5* segregated into distinct 3D chromatin association domains, displaying opposite sets of interactions with either transcriptionally inactive or active *Hoxa* or *Hoxb* genes, respectively (Figure 3A; Figure S3E).

We then compared the 3D chromatin conformations of *Hoxa* and *Hoxb* clusters after exogenous RA treatment at E9.5. In CC and *Hox5*-positive cells, RA treatment did not result in chromatin topological changes as compared to untreated cells (Figure 3C; Figures S3C, S3D, and S3G). In contrast, the chromatin interaction profiles in RA-treated *Hox5*-negative cells switched to a conformation similar to that normally displayed by the adjacent *Hox5*-positive

CellPress
OPEN ACCESS

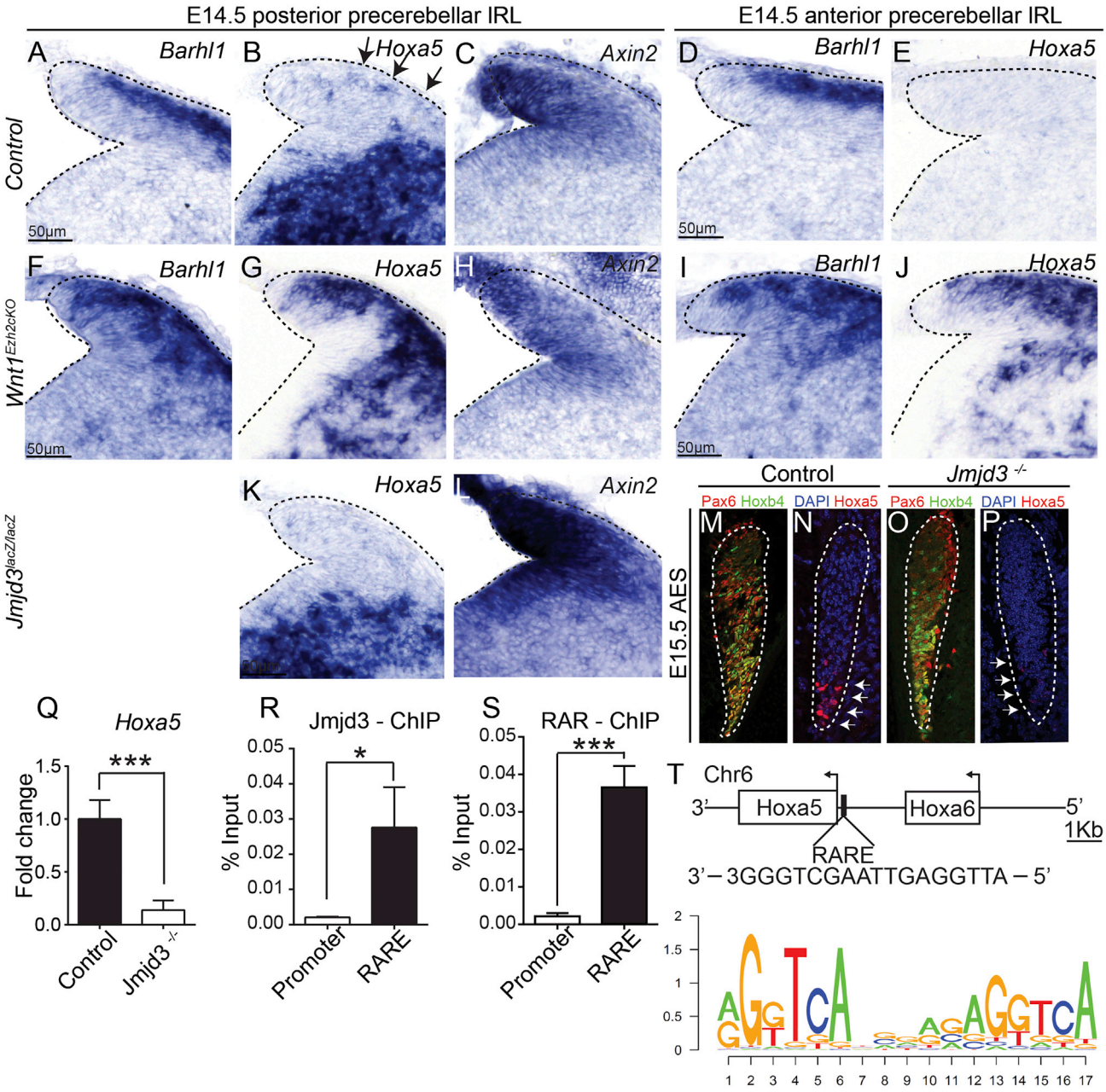

Figure 2. *Hox5* Transcriptional Induction in PN Neurons Requires Jmjd3

(A–L) E14.5 coronal sections of wild-type (A–E), *Wnt1*^{Ezh2cKO} (F–J), and *Jmjd3*$^{lacZ/lacZ}$ (K and L) showing expression of *Barhl1* (A, D, F, and I), *Hoxa5* (B, E, G, J, and K), and *Axin2* (C, H, and L) in anterior and posterior IRL (a-pIRL [D, E, I, and J] and p-IRL [A–C, F–H, K, and L], respectively. In *Wnt1*^{Ezh2cKO}, *Hoxa5* ectopically expands in postmitotic domains (G and J), correlating with increased *Barhl1* (F and I) and reduced *Axin2* expression (H); conversely, in *Jmjd3*$^{lacZ/lacZ}$, *Axin2* expression is expanded (L), and *Hoxa5* is not induced in postmitotic neurons (K).

(M–P) Pax6 and Hoxb4 (M and O) or Hoxa5 (N and P) expression on E15.5 AES of control (M and N) or *Jmjd3*$^{-/-}$ (O and P), showing strongly decreased Hoxa5 levels in *Jmjd3*$^{-/-}$ AES (arrows), while no change is observed for Hoxb4.

(Q) qPCR on FACS-isolated PN neurons from E18.5 control and *Atoh1(45)*^{tdTomato};*Jmjd3*$^{-/-}$ (n = 3; $p < 0.001$).

(R and S) ChIP-qPCR showing that Jmjd3 (R) and retinoic acid receptor (RAR) (S) bind to Hoxa5 RARE enhancer, but not promoter, in E14.5 hindbrain cells.

(T) Drawing illustrating position and sequence of the RARE with respect to *Hoxa5* and *Hoxa6* and JASPAR position weight matrix of Hoxa5 RARE. Data are presented as mean + SD.

See also Figure S2.

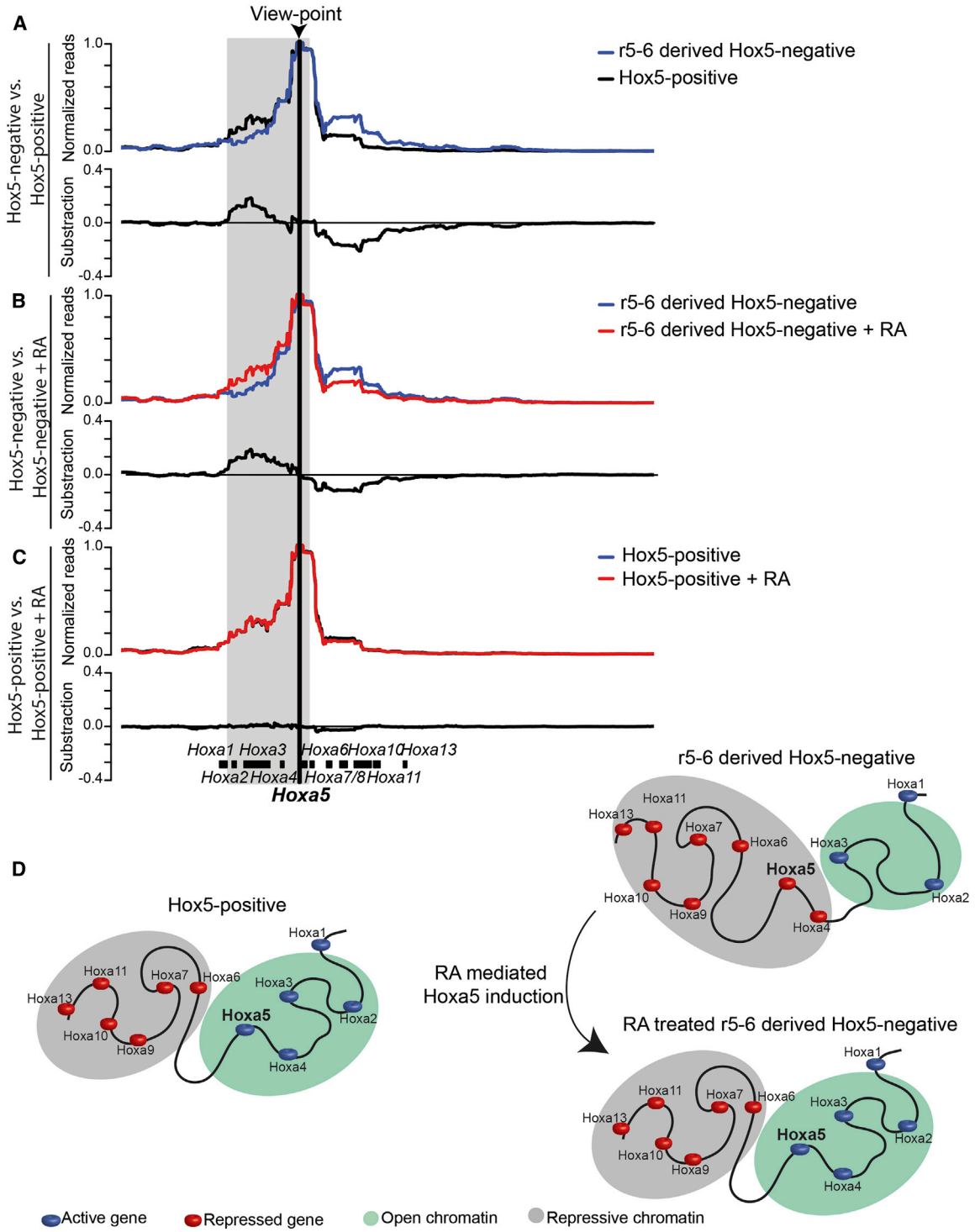

Figure 3. RA Signaling Regulates Higher Order Chromatin Configuration at *Hox5* Gene Loci

(A–C) Contact profiles of E14.5 r5- and r6-derived *Hox5*-negative and *Hox5*-positive hindbrain cells using the *Hoxa5* promoter as viewpoint (arrowhead) within a 400-kb window spanning the *Hoxa* cluster with or without RA treatment at E9.5. Substractions of the respective comparisons are depicted below normalized reads. (A) Rostrocaudal differences in association frequency of *Hoxa5* promoter with active or inactive domains within the *Hoxa* cluster. Exogenous RA leads to a 3D reorganization of chromatin conformation *in vivo* at the *Hoxa5* locus in (B) *Hox5*-negative, but not (C) *Hox5*-positive, samples. Note that (B) RA-treated *Hox5*-negative and (C) untreated *Hox5*-positive profiles are similar.

(D) Model of rostrocaudal RA-dependent chromatin reorganization at *Hoxa* cluster *in vivo*.

See also Figure S3.

cells, i.e., displaying less interactions with inactive and enhanced contacts with transcriptionally active *Hox* loci (Figures 3B and S3F).

In summary, chromatin conformation transitions at *Hox* loci can be induced in specific subpopulations of hindbrain neurons in a position-specific and context-dependent manner by their spatially restricted response to environmental RA (drawing in Figure 3D).

Hoxa5 Expression Is Sufficient to Drive Pontine Neuron Subsets into Posterior PNs

Hoxa5 is expressed in posterior subsets of PN neurons and maintained throughout migration and PN development. Thus, Hoxa5 could contribute to drive PN neurons to a posterior location in developing PNs. To test this hypothesis, we ectopically expressed Hoxa5 by *in utero* electroporation of E14.5 $ROSA^{CAG\text{-}lsl\text{-}Hoxa5\text{-}KI/lsl\text{-}tdTomato}$ (Table S1) IRL progenitors with *Cre*. Given the presence of a strong CAG promoter, the $ROSA^{CAG\text{-}lsl\text{-}Hoxa5\text{-}KI}$ line (STAR Methods) provides sustained Hoxa5 overexpression in a Cre-dependent manner. We compared the localization of *Cre*-electroporated, $tdTomato^+$ neurons in control $ROSA^{lsl\text{-}tdTomato}$ and $ROSA^{CAG\text{-}lsl\text{-}Hoxa5\text{-}KI/lsl\text{-}tdTomato}$ E18.5 PNs (Figures 4A–4D). In controls, $tdTomato^+$ neurons were spread throughout the anteroposterior axis (Figure 4A), whereas in $ROSA^{CAG\text{-}lsl\text{-}Hoxa5\text{-}KI/lsl\text{-}tdTomato}$, the anterior PN was devoided of $tdTomato^+$ neurons (Figures 4C and 4D). The posterior bias of Hoxa5-overexpressing PN neuron distribution was confirmed by quantification (Figure 4I).

To further support these results, we assessed the effect of Hoxa5 ectopic expression on the positioning of *Hox5*-negative PN neurons, using the tamoxifen (TM)-inducible $MafB^{tdTomato}$ line (Table S1). Following TM treatment at E7.5, 3D reconstructions of E18.5 and post-natal day (P)21 PNs (Figures 4J and S4A) showed that $tdTomato^+$ cells selectively localized to anterolateral and anteriormost positions. Next, we crossed $MafB^{tdTomato}$ with the Cre-dependent *Hoxa5*-overexpressing $ROSA^{lsl\text{-}Hoxa5\text{-}BAC}$ line and generated $MafB^{Hoxa5/tdTomato}$ mice (STAR Methods; Table S1). In $MafB^{Hoxa5/tdTomato}$ E18.5 fetuses and P21 mice, ectopic *Hoxa5*-expressing $tdTomato^+$ PN neurons lost their spatial restriction and spread toward posterior PNs (Figures 4K and S4B).

Unc5b Overexpression Rescues Mispositioning of Ectopic Hoxa5-Expressing PN Neurons

The *Unc5b* guidance receptor is required to maintain anterior IRL-derived PN neuron subsets in dorsal AES, whereas in ventral AES, *Unc5b* is repressed by Hox5 factors (Di Meglio et al., 2013). Thus, the posterior misplacement of anterior IRL-derived PN neurons ectopically overexpressing Hoxa5 might be partially explained by *Unc5b* downregulation during migration. We quantified *Unc5b* expression by RNA-FISH (fluorescence *in situ* hybridization) (STAR Methods) in the whole E15.5 AES of *Cre*-electroporated $ROSA^{CAG\text{-}lsl\text{-}Hoxa5\text{-}KI/lsl\text{-}tdTomato}$ and $ROSA^{lsl\text{-}tdTomato}$ as well as $MafB^{tdTomato}$ and $MafB^{Hoxa5/tdTomato}$ (Figures 4L–4M′, S4C, and S4D). We found significant reduction of *Unc5b* levels in both *Cre*-electroporated $ROSA^{CAG\text{-}lsl\text{-}Hoxa5\text{-}KI/lsl\text{-}tdTomato}$ and $MafB^{Hoxa5/tdTomato}$ AES (Figures 4N and S4E).

Next, we co-electroporated E14.5 IRL progenitors in $ROSA^{lsl\text{-}tdTomato}$ and $ROSA^{CAG\text{-}lsl\text{-}Hoxa5\text{-}KI/lsl\text{-}tdTomato}$ animals with *Unc5b* and *Cre*. Co-electroporated neurons overexpressing both Unc5b and Hoxa5 spread throughout the PN anteroposterior axis (Figures 4G and 4H), thus rescuing the mispositioning phenotype resulting from only Hoxa5 overexpression. Rescue was also confirmed by quantification (Figure 4I).

In summary, ectopic Hoxa5 expression in IRL-derived neurons is sufficient to drive them into the posterior PN, and this is, in part, achieved through *Unc5b* downregulation.

Relative Rostrocaudal Position of PN Neurons Is Predictive of Topographic Cortical Input

To investigate monosynaptic targeting of cortical axons onto PN neurons and the relationship between rostrocaudal location of PN neurons and patterned cortical input, we carried out trans-synaptic tracing (Wickersham et al., 2007; Callaway and Luo, 2015) of cortical cells from PN neurons (Figures 5A and 5B). To selectively infect PN neuron terminals in cerebellum, we used the TVA/EnvA cell-type-specific viral infection system (Beier et al., 2011; Osakada and Callaway, 2013) combined with *in utero* electroporation. We unilaterally electroporated E14.5 IRL progenitors with *rabies virus glycoprotein* and viral receptor *TVA* plasmids. Electroporation at this stage allows PN progenitors to be specifically targeted, since all other precerebellar mossy fiber nuclei have been already generated from the IRL (Altman and Bayer, 1987). At P2, we injected the mCherry EnvA-pseudotyped glycoprotein-deleted rabies virus, *EnvA-Rabies-ΔG-mCherry,* into the contralateral cerebellar hemisphere. Virus injection at this early stage resulted in widespread infection of the axon terminals of TVA-expressing neurons distributed throughout the rostrocaudal extent of the PNs (Figures 5C–5E). Rabies glycoprotein expression in these PN neurons (referred to as $WT^{TVA/EnvA/RabiesG}$) further allowed trans-synaptic tracing of monosynaptically connected neurons from cortical areas (Figure 5D).

In $WT^{TVA/EnvA/RabiesG}$ P8 brains, the majority of monosynaptically connected $mCherry^+$ neurons were in the $Ctip2^+$ cortical layer V ipsilateral to the electroporated PN neurons, while vGluT2 labeling of incoming thalamocortical axon terminals readily identified barrel cortex layer IV (Figures S5A–S5C). In addition, we found some labeled neurons in the contralateral cortical layer V, and several subcortical structures (Figures S5D–S5O), supporting previous analyses of PN input using non-trans-synaptic tracers (Kolmac et al., 1998; Mihailoff et al., 1989; Swenson et al., 1984; Terenzi et al., 1995). No cortical neurons were trans-synaptically labeled in non-electroporated animals (Figure 5C). 3D reconstruction of a representative whole cortex showed that cortical neurons projecting to PNs are distributed in all major motor and sensory areas (Figures 5E′ and 5I; STAR Methods for area contour mapping).

To assess the input connectivity of PN neuron subsets, we changed the placement of electroporation electrodes and selected anterior or posterior rhombic lip portions, thereby targeting neuron subsets with anterior or posterior PN distributions, respectively (Figures 5F and 5G). 3D reconstruction of the respective cortices revealed that monosynaptically connected neurons were regionally segregated (Figures 5F′ and 5G′). Transsynaptic tracing from neurons in anterior PNs resulted in labeling cortical neurons mostly in visual and motor areas (Figures 5F′ and 5I). Conversely, neurons in posterior PNs were mostly connected to somatosensory and motor areas (Figures 5G′ and 5I).

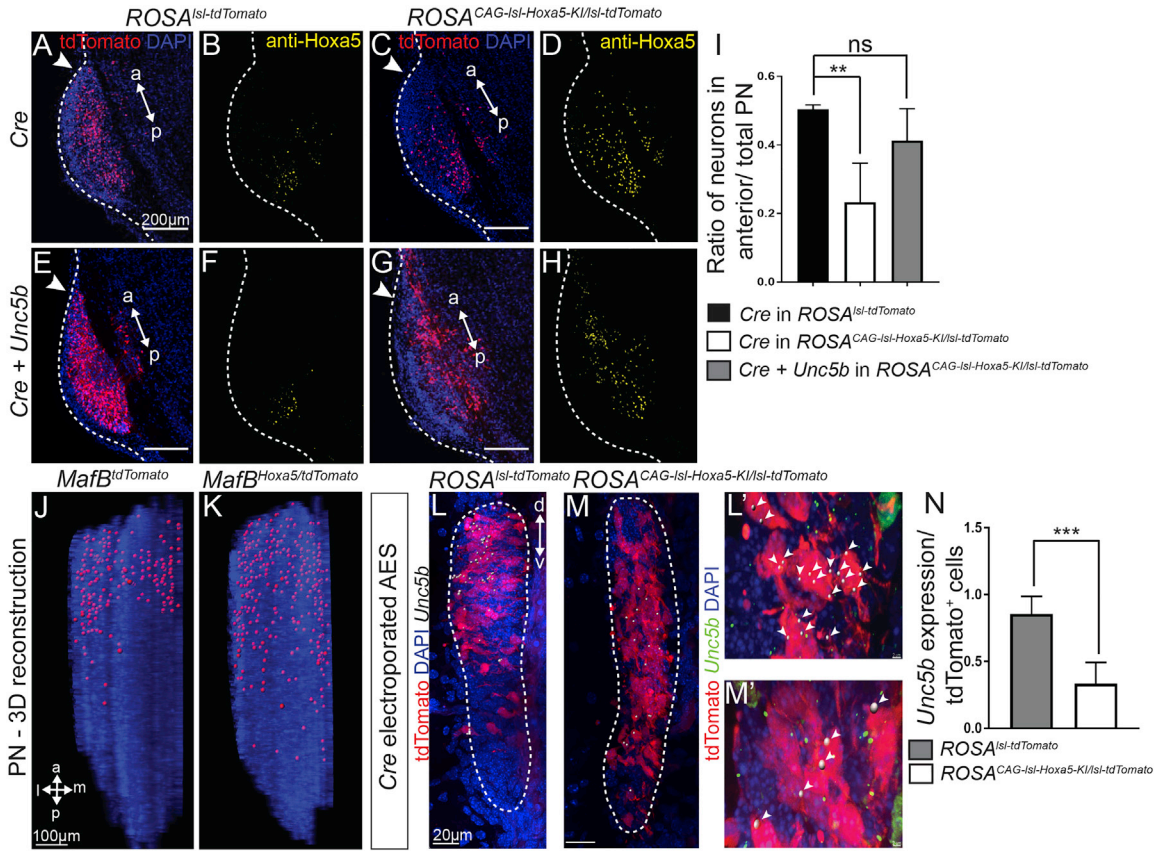

Figure 4. Hoxa5 Ectopic Expression Downregulates *Unc5b* and Drives Neurons to Posterior PNs

(A–H) E18.5 PN sagittal sections of *ROSA*$^{lsl\text{-}tdTomato}$ (A, B, E, and F) and *ROSA*$^{CAG\text{-}lsl\text{-}Hoxa5\text{-}KI/lsl\text{-}tdTomato}$ (C, D, G, and H) electroporated at E14.5 with *Cre* (A–D) or *Cre* and *Unc5b* (E–H). *Cre*-electroporated *ROSA*$^{lsl\text{-}tdTomato}$ tdTomato$^+$ PN neurons spread rostrocaudally (arrowhead, anterior PN) (A and E), whereas *ROSA*$^{CAG\text{-}lsl\text{-}Hoxa5\text{-}KI/lsl\text{-}tdTomato}$ Hoxa5-overexpressing tdTomato$^+$ neurons are mainly in the posterior PN (C); co-electroporated tdTomato$^+$ neurons spread throughout the anteroposterior extent of the PN (G), rescuing the posterior mispositioning of (C); (D and H) overexpression of Hoxa5 protein in *Cre*- (D) and *Cre*-plus-*Unc5b* (H)-electroporated *ROSA*$^{CAG\text{-}lsl\text{-}Hoxa5\text{-}KI/lsl\text{-}tdTomato}$ neurons.

(I) Bar graph of the ratio of anterior-to-total tdTomato$^+$ PN neurons (n = 4 for *Cre*; n = 3 for *Cre* and *Unc5b*; p = 0.005).

(J and K) 3D reconstruction of E18.5 *Mafb*^{tdTomato} (J) and *MafB*$^{Hoxa5/tdTomato}$ (K) PNs; tdTomato$^+$ neurons are indicated as red spots. *Mafb*^{tdTomato} neurons localize to anterolateral PNs in (J); upon ectopic Hoxa5 expression, neurons lose their spatial restriction and spread more posteriorly.

(L–M′) E15.5 AES, whole (L and M) or partial (L′ and M′), of E13.5 *Cre*-electroporated *ROSA*$^{lsl\text{-}tdTomato}$ (L and L′) and *ROSA*$^{CAG\text{-}lsl\text{-}Hoxa5\text{-}KI/lsl\text{-}tdTomato}$ (M and M′), showing tdTomato$^+$ neurons and *Unc5b* RNA-FISH. *Unc5b*-tdTomato$^+$ colocalization (arrowheads) is detected by IMARIS and indicated as spots. Reduced *Unc5b* expression is observed upon Hoxa5 ectopic expression.

(N) Bar graph of *Unc5b* expression per tdTomato$^+$ cells in E15.5 AES (n = 6 for *ROSA*$^{lsl\text{-}tdTomato}$; n = 5 for *ROSA*$^{CAG\text{-}lsl\text{-}Hoxa5\text{-}KI/lsl\text{-}tdTomato}$; p = 0.0002). Data are presented as mean + SD. a, anterior; p, posterior.

See also Figure S4.

Thus, the relative rostrocaudal position of PN neurons can be broadly predictive of monosynaptic topographic regional input from cerebral cortex.

Hoxa5-Expressing PN Neurons Are Preferentially Targeted by Subsets of Limb Somatosensory Cortical Neurons

Posterior PN neurons are preferentially connected to somatosensory cortical neurons (Figure 5; Leergaard and Bjaalie, 2007). Therefore, Hoxa5 expression in posterior subsets of PN neurons might orchestrate somatosensory specific input connectivity. We *in utero* co-electroporated *GFP* and *Cre* in E14.5 fetuses of homozygous females for *Tau*$^{lsl\text{-}RabiesG}$ (STAR Methods; Table S1), crossed with conditional *Hoxa5*-overexpressing *ROSA*$^{CAG\text{-}lsl\text{-}Hoxa5KI}$ heterozygous males (Figure S6A), and subsequently injected the *SAD-ΔG-mCherry* rabies virus (Osakada and Callaway, 2013) into their contralateral cerebellar hemisphere at P2; *ROSA*$^{CAG\text{-}lsl\text{-}Hoxa5\text{-}KI}$;*Tau*$^{lsl\text{-}RabiesG}$, *Cre*-electroporated, PN neurons overexpressed both *Hoxa5* and *rabies glycoprotein*, whereas *Tau*$^{lsl\text{-}RabiesG}$ *Cre*-electroporated neurons expressed only the *rabies glycoprotein* and served as controls.

In control *Cre*-electroporated *Tau*$^{lsl\text{-}RabiesG}$ cortex, mCherry$^+$ neurons were distributed in different cortical areas, including V1, S1, and M1 (Figures 6A′–6A‴) (see also Figure 5). In contrast, *Cre*-electroporated *ROSA*$^{CAG\text{-}lsl\text{-}Hoxa5\text{-}KI}$;*Tau*$^{lsl\text{-}RabiesG}$ PN neurons were preferentially distributed in posterior PN (Figures 6A

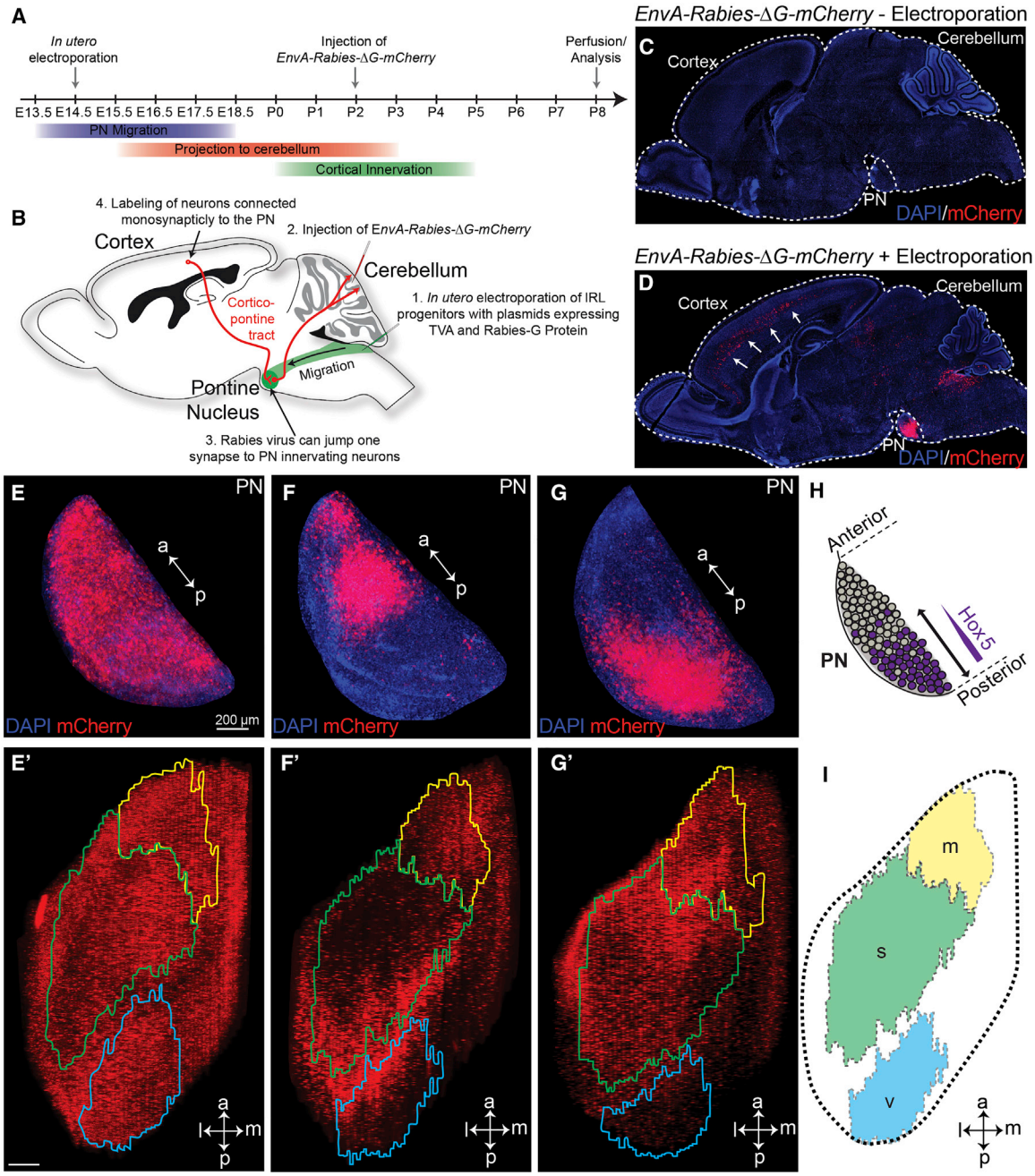

Figure 5. Rostrocaudal Position of PN Neurons Is Predictive of Cortical Input Connectivity

(A and B) Diagrams of experimental design for trans-synaptic tracing from PN neurons.

(C and D) P8 brain sagittal sections showing mCherry$^+$ neuron distributions following cerebellar *EnvA-Rabies-ΔG-mCherry* virus injection and infection of PN neurons, non-electroporated (C) or *in utero* co-electroporated with *Rabies-glycoprotein* and *TVA* at E14.5 (D). Only in co-electroporated PN neurons, *EnvA-Rabies-ΔG-mCherry* virus transynaptically traces monosynaptically connected cortical neurons (arrows in D). (C) and (D) are montages of tiled images.

(E–G′) 3D reconstructions of P8 $WT^{TVA/EnvA/RabiesG}$ PN (E–G) and respective ipsilateral cortices (E′–G′) showing infected neuron distribution after electroporation of whole (E and E′), anterior (F and F′), or posterior (G and G′) IRLs; single red spots indicate single mCherry$^+$ neurons. Color-coded contours label different cortical areas. Anterior PN neurons receive inputs mainly from visual and motor cortex (F and F′), whereas posterior PN neurons mainly from somatosensory and motor cortex (G and G′).

(H) Diagram of *Hox5* (purple) expression in the PN.

(I) Diagram of different color-coded 3D reconstructed cortical areas as in (F′). V, primary visual cortex (blue); S, primary somatosensory cortex (green); M, primary motor cortex (yellow); a, anterior; p, posterior; m, medial; l, lateral.

See also Figure S5.

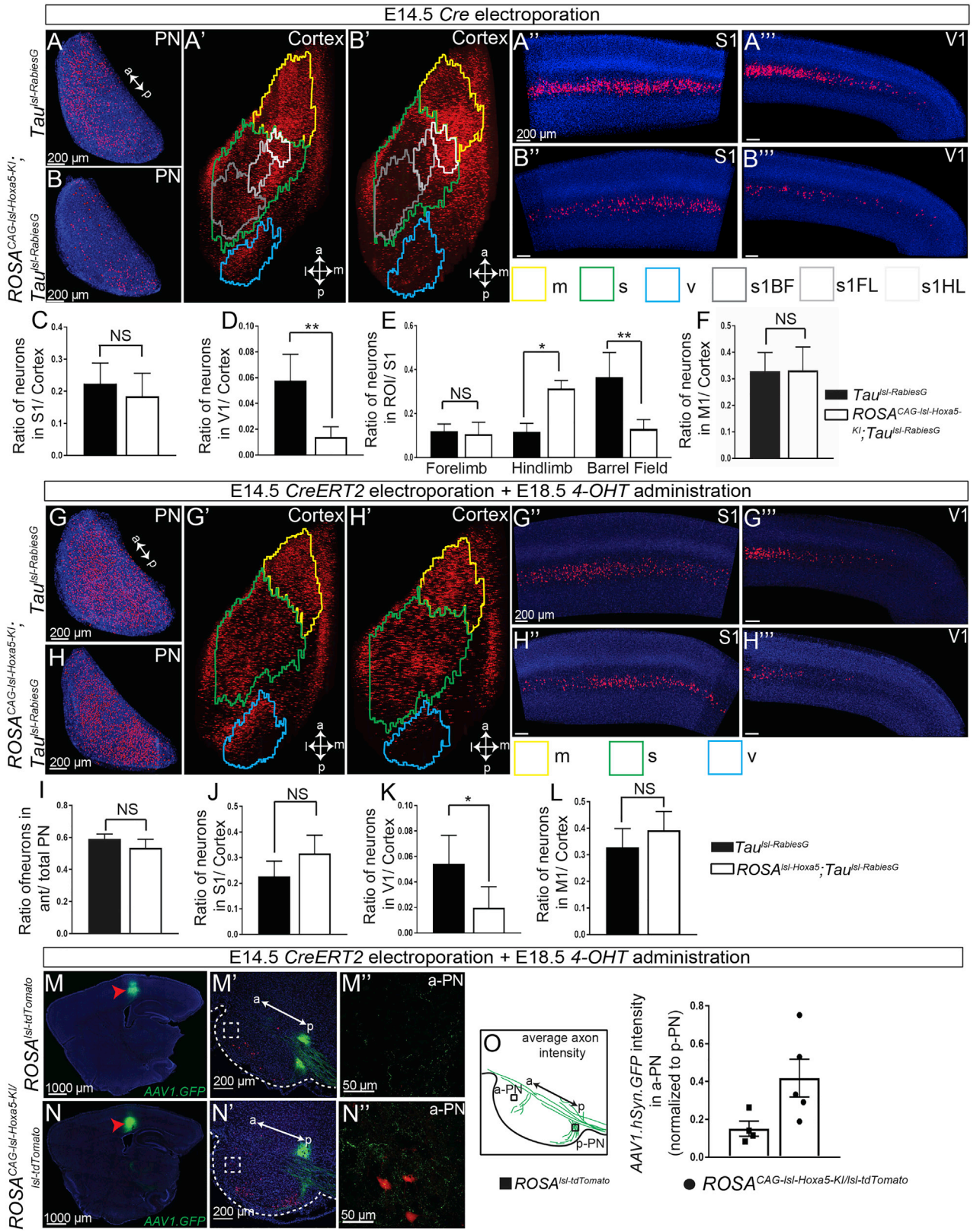

(legend on next page)

and 6B), supporting our previous findings (Figure 4), and received significantly reduced monosynaptic input from V1 (Figures 6B′, 6B‴, 6D, and S5P), while no significant change was observed for S1 or M1 input (Figures 6B′, 6B″, 6C, 6F, and S5P).

In addition to regional representation of distinct cortical areas in the PN, the S1 sensory body representation is also generally mapped in a topographic manner onto the central-posterior PN. Namely, axons from S1 whisker (barrel) or face-mapping regions project rostrally to limb-specific cortical projections, which project more posteriorly in the PN, thus preserving cortical topography (Brodal, 1968; Mihailoff et al., 1978; Wiesendanger and Wiesendanger, 1982; Kosinski et al., 1986; Panto et al., 1995; Leergaard et al., 2000b). Quantification of mCherry$^+$ neurons in forelimb, hindlimb, and barrel S1 cortex in *Cre*-electroporated *Tau$^{lsl\text{-}RabiesG}$* and *ROSA$^{CAG\text{-}lsl\text{-}Hoxa5\text{-}KI}$;Tau$^{lsl\text{-}RabiesG}$* brains showed that Hoxa5 expressing neurons were preferentially innervated by limb rather than barrel somatosensory cortical axon input (Figure 6E).

Hoxa5 Expression Instructs Cortical Somatosensory Inputs at the Expense of Visual Inputs Regardless of PN Neuron Position

The enrichment of limb somatosensory inputs and paucity of visual cortical inputs synapsing with Hoxa5-expressing PN neurons could be expected by their posterior position in the PN. To distinguish an additional Hoxa5 role, besides driving neurons to posterior PNs, in selecting specific subsets of cortical inputs regardless of neuron position, we modified our trans-synaptic tracing strategy (Figure S6B). Expression of *rabies glycoprotein* only, or of both *rabies glycoprotein* and Hoxa5, was induced in postmigratory, E14.5 *in utero CreERT2*-electroporated, *Tau$^{lsl\text{-}RabiesG}$* or *ROSA$^{CAG\text{-}lsl\text{-}Hoxa5\text{-}KI}$;Tau$^{lsl\text{-}RabiesG}$* PN neurons, respectively, by administering TM at E18.5; the *SAD-ΔG-mCherry* rabies virus was then injected in contralateral cerebellum at P2.

Unlike Hoxa5 overexpression at the premigratory stage causing a posterior bias of Hoxa5+ neuron position in the PN (Figures 4 and 6B), no rostrocaudal positional bias was observed at P8 for *ROSA$^{CAG\text{-}lsl\text{-}Hoxa5\text{-}KI}$;Tau$^{lsl\text{-}RabiesG}$* *CreERT2*-electroporated neurons (Figures 6G, 6H, and 6I). Hoxa5-overexpressing neurons in *CreERT2*-electroporated *ROSA$^{CAG\text{-}lsl\text{-}Hoxa5\text{-}KI}$;Tau$^{lsl\text{-}RabiesG}$* received reduced input from V1 as compared to control neurons in *CreERT2*-electroporated *Tau$^{lsl\text{-}RabiesG}$* (Figures 6G′, G‴, H′, H‴, K, and S5Q). As V1 axon collaterals only enter the rostral portion of the PN (Mihailoff et al., 1984; O'Leary and Terashima, 1988), this finding strongly suggests that anteriorly located PN neurons ectopically expressing Hoxa5 inhibit their targeting by V1 axon collaterals. On the other hand, we observed no significant change in the fraction of monosynaptically connected neurons from S1 and M1 (Figures 6G″, 6H″, 6J, and 6L), suggesting that Hoxa5-expressing neurons can be targeted by S1 axon collaterals regardless of position in the PN.

We next carried out cortical axon tracing using anterograde adeno-associated virus (AAV) (Figure S6C). E14.5 *CreERT2*-electroporated *ROSA$^{lsl\text{-}tdTomato}$* and *ROSA$^{CAG\text{-}lsl\text{-}Hoxa5\text{-}KI/lsl\text{-}tdTomato}$* served as control and experimental sets, respectively. TM was administered at E18.5. At P5, we injected AAV1.hSyn.eGFP (Harris et al., 2012) in S1 to trace cortical inputs to the PN. Upon postmigratory Hoxa5 overexpression throughout the PN rostrocaudal extent, we observed increased S1 axon terminals in anterior PNs (Figures 6M″, 6N″, and 6O), strongly indicating that Hoxa5-expressing neurons are instructive for attracting somatosensory input.

In summary, Hoxa5 has successive roles in developing PN neurons. Early Hoxa5 expression in migrating neurons guides them to posterior PNs; Hoxa5-expressing subsets will thus

Figure 6. Hoxa5 Expression Is Sufficient to Organize Input Connectivity of PN Neurons

(A–B‴) P8 sagittal sections of E14.5 *Cre*-electroporated *Tau$^{lsl\text{-}RabiesG}$* (A) and *ROSA$^{CAG\text{-}lsl\text{-}Hoxa5\text{-}KI}$;Tau$^{lsl\text{-}RabiesG}$* (B) samples showing distribution of electroporated neurons in the PN (GFP+ in red) (A and B) and trans-synaptically traced mCherry$^+$ neurons in distinct areas of respective ipsilateral cortices (A′ and B′), and S1 (A″ and A‴) and V1 (B″ and B‴) following P2 cerebellar injection of *SAD- ΔG-mCherry* virus.

(C–F) Bar graph of fraction of mCherry$^+$ neurons in S1 (C), in V1 (D), within distinct S1 regions (E), and in M1 (F) (n = 7 for *Tau$^{lsl\text{-}RabiesG}$*; n = 5 for *ROSA$^{CAG\text{-}lsl\text{-}Hoxa5\text{-}KI}$;Tau$^{lsl\text{-}RabiesG}$*); p values are 0.348 (C), 0.001 (D), 0.974 (E, forelimb), <0.0001 (E, hindlimb), <0.0001 (E, barrel field), and 0.955 (F), respectively. Posteriorly biased, Hoxa5-overexpressing PN neurons receive reduced input from V1 and barrel S1 and enriched input from hindlimb S1.

(G–H‴) P8 sagittal sections of E14.5 *CreERT2*-electroporated *Tau$^{lsl\text{-}RabiesG}$* (G) and *ROSA$^{CAG\text{-}lsl\text{-}Hoxa5\text{-}KI}$;Tau$^{lsl\text{-}RabiesG}$* (H) showing distribution of PN electroporated neurons (GFP+ in red) (G and H) and trans-synaptically traced mCherry$^+$ neurons in distinct areas of respective ipsilateral cortices (G′ and H′), and S1 (G″ and H″) and V1 (G‴ and H‴) following TM-induced *CreERT2*-mediated Hoxa5 and Rabies-glycoprotein ectopic activation at E18.5 and P2 cerebellar injection of *SAD-ΔG-mCherry*.

(I–L) Bar graph of fraction of mCherry$^+$ neurons in anterior PN (I), S1 (J), V1 (K), and M1 (L) (n = 4 for *Tau$^{lsl\text{-}RabiesG}$*; n = 7 for *ROSA$^{CAG\text{-}lsl\text{-}Hoxa5\text{-}KI}$;Tau$^{lsl\text{-}RabiesG}$*); p values are 0.089 (I), 0.063 (J), 0.016 (K), and 0.214 (L). Regardless of their rostrocaudal position, postmigratory PN neurons ectopically overexpressing Hoxa5 are still targeted by S1 but receive reduced V1 inputs.

(M–N″) P18 sagittal sections of E14.5 *CreERT2*-electroporated *ROSA$^{lsl\text{-}tdTomato}$* (M–M″) and *ROSA$^{CAG\text{-}lsl\text{-}Hoxa5\text{-}KI/lsl\text{-}tdTomato}$* (N–N″) brains cortically injected with *AAV1.hSyn.eGFP* at P5 after TM-induced CreERT2 activation at E18.5. (M and N) Whole cortex sections indicating injection site (red arrowhead). (M′ and N′) PN sagittal sections showing cortical axon bundles (green) and tdTomato$^+$ electroporated neurons (red). (M″ and N″) Higher magnification of anterior PN (a-PN) neurons from the insets in (M′) and (N′). S1 afferents project to posterior PNs (p-PN), with very few collaterals present in a-PN (M″); upon postmigratory Hoxa5 ectopic expression, S1 input targeting a-PN is increased (N″). (M) and (N) are montages of tiled images.

(O) Quantification of the S1 projections in the anterior PN (a-PN) in TM-treated, *AAV1.hSyn.eGFP*-injected, *CreERT2*-electroporated *ROSA$^{lsl\text{-}tdTomato}$* and *ROSA$^{CAG\text{-}lsl\text{-}Hoxa5\text{-}KI/lsl\text{-}tdTomato}$* animals. Bar graph of ratio of GFP signal intensity in a-PN normalized to the posterior PN (p-PN) (p = 0.058). Each point represents quantification from individual animals. Data are presented as mean + SD. PN and cortex representations are 3D reconstructions. S1 and V1 images are 3D reconstructions of a stack of 5 consecutive sagittal sections. Contour color and legend: m, motor (yellow); s, somatosensory (green); v, visual (blue); S1BF, primary somatosensory barrel field (dark gray); S1FL, S1 forelimb (light gray); S1HL, S1 hindlimb (white). a, anterior; p, posterior; m, medial; l, lateral; S1, primary somatosensory cortex; V1, primary visual cortex; M1, primary motor cortex.

See also Figures S5 and S6.

have higher probability to be targeted by topographically arranged somatosensory afferents of the corticospinal tract. We further reveal that Hoxa5 expression in randomly selected subsets of anterior PN neurons after their migration is instructive to integrate them in a specific connectivity sub-network relaying mainly somatosensory information while avoiding visual input.

Transcriptional Programs of Hoxa5 Expressing PN Neurons

To identify genes potentially involved in circuit formation downstream *Hox5* genes, we carried out RNA sequencing (RNA-seq) and comparative transcriptome analysis on the whole PN as well as distinct subsets of PN neurons, isolated by FACS from Cre-dependent reporter-expressing lines. We used the *Atoh1(45)::Cre* driver, since in *Atoh1(45)*^{tdTomato} mice, tdTomato expression is only detected in postmitotic lRL-derived neurons starting at migration onset and distributed throughout the AES at E14.5 and the PN at P0 (Figures S7A–S7D).

We compared RNA-seq datasets of PN neurons isolated from E18.5 *Atoh1(45)*^{tdTomato} and *Hoxa5*^{tdTomato} animals (Figures 7A and 7B) and identified 637 differentially expressed genes (fold change [FC] > 1.5; false discovery rate [FDR] < 0.07), among which 456 (72%) were upregulated and 181 (28%) were downregulated (Figure 7E). As expected, *Hoxa5*, *Hoxb5*, and *Hoxc5* were enriched in the *Hoxa5*^{tdTomato} versus *Atoh1(45)*^{tdTomato} samples.

We next compared the RNA-seq profiles of *Atoh1(45)*^{tdTomato} and *Atoh1(45)*^{Hoxa5} (Table S1) E18.5 PN neurons (Figure 7C). In *Atoh1(45)*^{Hoxa5}, both GFP (as a proxy for Hoxa5 overexpression) and Hoxa5 were readily detected in PN neurons at P0 (Figures 7D and S7O). We found 736 genes differentially expressed, with 306 (42%) being upregulated and 430 (58%) being downregulated in the *Atoh1(45)*^{Hoxa5} versus *Atoh1(45)*^{tdTomato} samples, respectively (Figure 7F). No other *Hox5* paralog gene showed significant changes in their expression, indicating that Hoxa5 does not cross-regulate *Hox5* paralogs in PN neurons.

We next asked which genes were similarly expressed in *Hoxa5*^{tdTomato} versus *Atoh1(45)*^{tdTomato} (i.e., endogenous *Hox5*-expressing) and *Atoh1(45)*^{Hoxa5} versus *Atoh1(45)*^{tdTomato} (i.e., *Hoxa5*-overexpressing) neuron subsets. We found a highly significant genome-wide correlation ($r = 0.18$, $p < 0.0001$) between endogenous and overexpressing Hoxa5 PN subpopulations, respectively (Figure 7J). We found 145 genes whose expression pattern was shared, of which 107 (74%) were upregulated and 38 (26%) downregulated in both populations (Figures 7G and 7H). On the other hand, when comparing *Atoh1(45)*^{tdTomato} (whole PN) versus *Hoxa5*^{tdTomato} or *Atoh1(45)*^{tdTomato} versus *Atoh1(45)*^{Hoxa5}, many genes were differentially regulated in both comparisons (Figure 7I). Gene Ontology (GO) analysis revealed genes critical for biological processes involved in topographic circuit formation, such as cell adhesion, axon guidance, and chemotaxis (Figure 7I).

To uncover Hox5-dependent rostrocaudal molecular gradients within the developing PN, we next analyzed the expression pattern of differentially expressed genes in *Atoh1(45)*^{tdTomato} versus *Atoh1(45)*^{Hoxa5} RNA-seq assays. We screened the Allen Mouse Brain Atlas (Lein et al., 2007) (http://mouse.brain-map.org) and the Allen Developing Mouse Brain Atlas (http://developingmouse.brain-map.org) for wild-type expression of *Epha3*, *Pcdh19*, *Peg10*, *Cdhr1*, *Ephb1*, *Nrp1*, *Sfrp4*, *chl1*, *St18*, and *Sox11* (Figures S7E–S7N). These genes displayed rostrocaudally graded or spatially restricted expression, supporting our experimental approach. We additionally assessed the expression of a further set of differentially expressed genes; namely, *Crabp1*, *Nrp2*, *Slit3*, *Clb1*, *Lmo3*, and *SST*. *Crabp1* and *SST* were downregulated (Figures S7Q and S7R), while *Nrp2*, *Slit3*, *Clb1*, and *Lmo3* were upregulated upon Hoxa5 overexpression (Figures S7S–S7V), thus validating them as Hoxa5 downstream targets in PN neurons.

In summary, comparative transcriptome analysis revealed the existence of molecular gradients within the PN, in part regulated by Hoxa5, potentially contributing to specification and connectivity.

DISCUSSION

During brain development, a stereotypic sequence of neuronal specification, ordered migration, establishment of axonal wiring, and synaptic connectivity needs to be tightly regulated in space and time to achieve meaningful topographic circuit assembly. However, whether and how individual transcription factors are able to collectively coordinate these successive processes remain still largely unknown. Here, we used a comprehensive genetic approach coupled with *in utero* electroporation and *in vivo* trans-synaptic tracing and showed that Hox5 transcription factors are involved in coordinating the specification and orderly positioning of distinct precerebellar neuron subsets in the developing PN and in orchestrating their topographic input connectivity from distinct cortical neuron subsets in position-dependent and -independent manners.

Rostrocaudal specification of neuronal identities requires Hox activity (Studer et al., 1996; Gavalas et al., 1997; Gavalas et al., 1998; Davenne et al., 1999; Dasen et al., 2003; Oury et al., 2006; Narita and Rijli, 2009; Tümpel et al., 2009; Philippidou and Dasen, 2013; Bechara et al., 2015). *Hox* spatiotemporal regulation in progenitor and/or postmitotic neurons involves an interplay between local signaling, dynamic chromatin changes, and transcriptional output. How these processes are integrated *in vivo* during cell-fate specification is poorly understood. Here, we found that the response to RA of postmitotic PN neurons is spatially graded so that only posterior-rhombic-lip-derived neurons are able to respond (Figure 1). *Hox5* gene induction is spatially restricted to these posterior RA-responsive subsets. In pontine neurons, *Hoxa5* and *Hoxb5* display distinct spatial expression limits in the lRL (Figure S1), which may reflect distinct responses to rostrocaudal RA levels from meninges. Dynamic patterns of transcription and associated chromatin changes at *Hox5* loci have been investigated during RA-mediated embryonic stem cell differentiation (Kashyap et al., 2011; Mazzoni et al., 2013; De Kumar et al., 2015). Indeed, *Hoxa5* and *Hoxb5* respond to RA through specific RAREs (Chen et al., 2007) and display distinct transcriptional responses implemented through different mechanisms involving the elongation of paused RNA polymerase II (RNA Pol II) or rapid recruitment of RNA Pol II and transcriptional initiation (Lin et al., 2011; De Kumar et al., 2015).

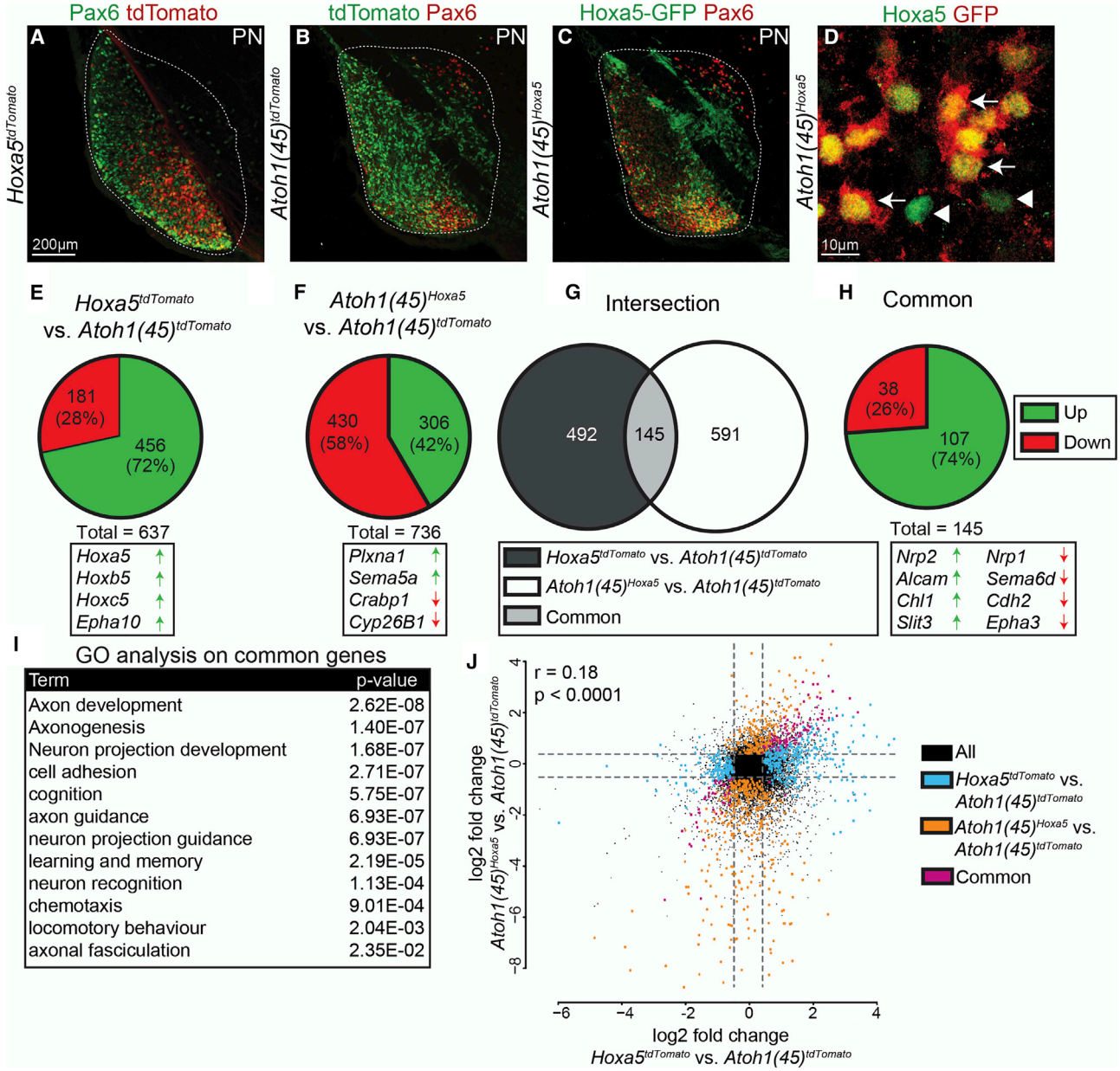

Term	p-value
Axon development	2.62E-08
Axonogenesis	1.40E-07
Neuron projection development	1.68E-07
cell adhesion	2.71E-07
cognition	5.75E-07
axon guidance	6.93E-07
neuron projection guidance	6.93E-07
learning and memory	2.19E-05
neuron recognition	1.13E-04
chemotaxis	9.01E-04
locomotory behaviour	2.04E-03
axonal fasciculation	2.35E-02

Figure 7. Transcriptional Programs of *Hoxa5*-Expressing PN Neurons

(A–C) E18.5 PN sagittal sections showing Pax6 (green) and tdTomato (red) expression in *Hoxa5*^{tdTomato} (A) and *Atoh1(45)*^{tdTomato} (B) samples and Pax6 (red) and GFP (green) in *Atoh1(45)*^{Hoxa5} (C) samples.

(D) Higher magnification of PN neurons in *Atoh1(45)*^{Hoxa5} samples showing co-expression of Hoxa5 (green) and GFP (red) (arrows). A few Hoxa5^{+}/GFP^{-} cells were also seen (arrowheads).

(E–H) Pie charts showing genes regulated in *Hoxa5*$^{+}$ (E), Hoxa5-overexpressing (F), and commonly regulated genes (H) as assessed by E18.5 RNA-seq of PN neurons FACS isolated from *Atoh1(45)*^{tdTomato}, *Hoxa5*^{tdTomato}, and *Atoh1(45)*^{Hoxa5} samples (FC > 1.5; FDR < 0.07). Examples of genes and their regulation are in the boxes below the respective pie charts. (G) Venn diagram showing the intersection between *Hoxa5*^{tdTomato} versus *Atoh1(45)*^{tdTomato} and *Atoh11(45)*^{Hoxa5} versus *Atoh1(45)*^{tdTomato} RNA-seq comparisons.

(I) GO analysis of commonly regulated genes.

(J) Scatterplot showing significant correlation between *Hoxa5*^{tdTomato} versus *Atoh1(45)*^{tdTomato} and *Atoh11(45)*^{Hoxa5} versus *Atoh1(45)*^{tdTomato} RNA-seq comparisons (r = 0.19; R^2 = 0.036; p < 0.0001). Data are presented as mean + SD.

See also Figure S7.

RA-dependent *Hox5* transcriptional output is accompanied by region-specific chromatin regulation along the rostrocaudal axis (Figure 2). In *Ezh2* null mutants, similarly to wild-type mice treated with exogenous RA, *Hox5* genes are derepressed throughout the AES (Di Meglio et al., 2013), indicating increased sensitivity of *Ezh2*-depleted neurons to endogenous RA levels along the rostrocaudal axis. Thus, the *Ezh2*/H3K27me3 repressive mark may attenuate the transcriptional response of *Hox5* genes to endogenous RA, setting a threshold that can only be overcome in the posterior rhombic lip due to higher endogenous RA levels. *Ezh2*/H3K27me3 depletion is not by itself sufficient for strong *Hox5* induction, which requires RA-induced transcriptional response. In *Ezh2* mutants, *Hox5* genes are not ectopically induced in the *Axin2*$^{+}$/*Wnt1*$^{+}$ mitotic progenitor compartment, which appears reduced in *Ezh2* null mutants (Figure 2). Moreover, the *Wnt1*$^{+}$ rhombic lip appears to be unresponsive to RA signaling from the meninges, as assessed in *RARE*^{lacZ} reporter mice (Figures 1 and S1). A mutually negative regulation has been shown between Wnt signaling, which maintains intestinal stem cells, and RA-induced HOXA5, which drives their differentiation (Ordóñez-Morán et al., 2015), suggesting that a similar mechanism might be at work for *Hox5* expression in the *Wnt1*$^{+}$ lRL mitotic domain.

H3K27me3 depletion at developmentally regulated genes, including *Hox* genes, requires UTX and/or Jmjd3 demethylases (Burchfield et al., 2015). *Jmjd3*, in particular, is involved in the regulation of neurogenesis (Ramadoss et al., 2012; Jiang et al., 2013; Kartikasari et al., 2013). However, little is known about how specific demethylases contribute to spatially restricted specification of neuronal subtype identity *in vivo* in response to rostrocaudal signals. We show that *Jmjd3* expression levels are strongly enhanced in pontine postmitotic neurons from the onset of migration (Figure S1) and that *Jmjd3* is necessary to achieve optimal RA-induced *Hox5* transcriptional levels at the onset and during migration (Figure 2). Together with RARa, Jmjd3 is recruited to directly bind a *Hoxa5* RARE, in keeping with a role of Jmjd3 at neural enhancers and promoters (Park et al., 2014), suggesting that it directly contributes to switching from poised to active enhancer state.

Lastly, *Hox* cluster higher order chromatin conformation is dynamic during development and differentiation (Noordermeer et al., 2011; Chambeyron and Bickmore, 2004; Ferraiuolo et al., 2010; Rousseau et al., 2014). However, the role of environmental signals in driving region-specific chromatin changes at *Hox* clusters during neuronal development remains poorly understood. We found that RA signaling is instructive for topographic transitions of *Hox* cluster chromatin 3D conformation along the hindbrain rostrocaudal axis (Figure 3).

Establishment of topographic maps requires multiple processes, including prenatal interactions of molecular gradient cues, axonal and dendritic remodeling, and experience-dependent refinement during early postnatal critical periods (Cang and Feldheim, 2013). In the developing corticopontine circuit, somatosensory cortical axon collaterals target a broad centrocaudal region in the PN and are further refined to attain the adult regional targeting pattern in the PN (Mihailoff et al., 1984). In contrast, visual cortical neuron axon collaterals only target the anterior PN (Stanfield and O'Leary, 1985; O'Leary and Terashima, 1988). At a larger scale, pontine neuron dendritic fields remain constrained within the area targeted by a single cortical region (Schwarz and Thier, 1995; Schwarz et al., 2005), leading to the suggestion that regional cortical topography is largely preserved in the PN. When cortical input from somatosensory or motor cortex is removed, then cortical visual axon collaterals can innervate posterior PN neurons (O'Leary et al., 1991). This suggests that distinct post-synaptic PN neuron subsets may provide both permissive and instructive cues that ultimately contribute to determine the topography and specificity of presynaptic cortical afferent targeting.

By trans-synaptic tracing, we provide here direct demonstration that broad regional topography of cortical connectivity is maintained in the PN. A main finding is that the settling position of pontine neurons along the PN rostrocaudal axis can be broadly predictive of input from distinct sensory cortical areas. For instance, pontine neurons in the centrocaudal PN display enriched somatosensory, at the expense of visual, cortical input (Figure 5). At a finer scale, clusters of corticopontine projections mapping the same body part distributed within inside-out concentric layers or "lamellae," generating multiple somatosensory body maps in centrocaudal PNs (Leergaard and Bjaalie, 1995; Leergaard et al., 2000a, 2000b, 2004). This organization was speculated to relate to the inside-out gradient of pontine neuron birthdating (Altman and Bayer, 1987) and temporal internal-to-external corticopontine projection pattern observed in newborns and further refined through adult stages (Leergaard et al., 1995). However, temporal and maturational gradients cannot fully explain the complexity of the fine-grained somatotopic connectivity pattern between cortical input and pontine neuron targets. One possibility is that both the position and specific intrinsic molecular programs of post-synaptic PN neurons contribute to this complex cortico-pontine input connectivity pattern.

The contributions of neuronal settling position versus intrinsic molecular identity in the establishment of complex input-output wiring diagrams is beginning to emerge during the assembly of spinal motor circuits (Jessell et al., 2011; Sürmeli et al., 2011; Tripodi et al., 2011; Levine et al., 2012; Bikoff et al., 2016; Baek et al., 2017). Similarly, in the developing neocortex, certain transcription factors can concomitantly regulate neuronal migration and final position with the acquisition of laminar subtype identity and connectivity (Kwan et al., 2008). In this study, we investigated whether similar principles might apply during corticopontine circuit development. We found that Hoxa5 is required to couple both positional information and intrinsic molecular identity to determine specific cortical somatosensory afferent connectivity in the PN. Because of their final posterior position in the PN, Hoxa5^{+} neurons have a higher probability to connect to somatosensory than visual cortical input (Figures 5 and 6). On the other hand, we additionally found that Hoxa5^{+} neurons preferentially connect with limb, rather than face/whisker, somatosensory cortical neurons (Figures 5 and 6). This suggested that Hoxa5 expression, in addition to driving neurons to posterior PNs, could be sufficient to instruct a molecular program selecting cortical input specificity. To uncouple this potential additional role of Hoxa5, regardless of PN neuron position, we overexpressed Hoxa5 after PN neuron migration and settling. We found

that post-migratory neurons ectopically expressing Hoxa5 throughout the PN rostrocaudal axis preferentially connect to S1 and avoid V1 cortical neurons (Figure 6). Moreover, anteriorly located ectopically Hoxa5-expressing PN neurons were able to ectopically attract S1 somatosensory axons (Figure 6).

It is noteworthy that Hoxa5 expression in pontine neurons is sufficient to restrict targeting by V1 cortical axons and bias the input of S1 axons toward limb, rather than face, representations. Other *Hox* paralog group genes, i.e., *Hox2-4* genes, might provide molecular and positional identities to PN neurons to acquire their main input. In this respect, *Hoxa2* ectopic expression in the brainstem dorsal principal trigeminal nucleus (dPrV) was sufficient to attract peripheral whisker-related sensory afferents and generate ectopic barrelettes at the expense of mandibular somatosensory input (Bechara et al., 2015). Within the centrocaudal somatosensory PN, pontine neuron subsets might, therefore, establish Hox-dependent transcriptional sub-programs to determine the specificity of innervation of distinct subsets of incoming cortical somatosensory axons. Indeed, downstream of Hoxa5 several genes are involved in axon refinement and pathfinding (Figure 7), potentially assisting in cortico-pontine connectivity.

Lastly, a main limitation of this study is that it primarily relies on gain-of-function data. On the other hand, it is highly likely that the effects of single *Hox5* gene deletions would be largely compensated *in vivo* by functional redundancy from the other paralogs. Thus, rather than studying unique and shared functions of individual Hox5 paralog genes in conditional compound mutant precerebellar neurons, which would have been technically unfeasible in the mouse, we used here a comprehensive genetic, cellular, and molecular *in vivo* approach to show that a single Hox5 factor is sufficient to regulate specific aspects of precerebellar neuron specification, migration, and connectivity.

In conclusion, we provide here critical insights into the developmental mechanisms establishing cortico-pontine somatosensory maps and improve our understanding of the molecular logic underlying Hox-dependent sub-circuit specialization during development.

STAR★METHODS

Detailed methods are provided in the online version of this paper and include the following:

- KEY RESOURCES TABLE
- RESOURCE AVAILABILITY
  - Lead Contact
  - Materials Availability
  - Data and Code Availability
- EXPERIMENTAL MODEL AND SUBJECT DETAILS
  - Mouse Genetics
  - Generation of the Atoh1(45)::Cre line
  - Generation of the Jmjd3 knock-in line
  - Generation of the ROSA26::(lox-stop-lox)Hoxa5-IRES-GFP BAC transgenic line
  - Generation of the ROSA26::CAG(lox-stop-lox)3xFlag-Hoxa5-IRES-GFP knock-in line
  - Generation of the Tau::(lox-stop-lox)Rabies-glycoprotein-IRES-nls-lacZ
  - Generation of Hoxa5::Cre knock-in line
- METHOD DETAILS
  - Tissue sectioning
  - Immunohistochemistry
  - *In Situ* Hybridization
  - RNA-FISH
  - *In vivo* treatment
  - In utero electroporation
  - Fluorescent activated Cell Sorting (FACS)
  - Quantitative PCR (qPCR)
  - Chromatin immunoprecipitation (ChIP)
  - 4C template preparation
  - 4C PCR, mapping and analysis of 4C data
  - RNA sequencing analysis
  - Virus production and tracing experiments
  - Imaging, 3D-reconstructions and Image processing
- QUANTIFICATION AND STATISTICAL ANALYSIS

SUPPLEMENTAL INFORMATION

Supplemental Information can be found online at https://doi.org/10.1016/j.celrep.2020.107767.

ACKNOWLEDGMENTS

We are grateful to D. Saur for mouse lines; E. Callaway for viruses; B. Roska for electroporation plasmids; P. Bovolenta, P. Dollé, and A. Chédotal for in situ hybridization probes; K. Karmakar for help with setting up the trans-synaptic rabies tracing experiment; D. Machlab for the position weight matrix of Hoxa5 RARE; and S. Jin and R. Nitschke for providing and teaching the LIC macro for tile recording with Zeiss Zen 2010 software. We thank the FMI imaging, genomics, and animal facilities for excellent technical support and T. Roloff for RNA sequencing. T.D.M. was an EMBO LT Fellowship recipient. N.A.M. was funded by Marie Curie IEF (FP7-PEOPLE-2013). Work in the F.M.R. laboratory was supported by the Swiss National Science Foundation (31003A_149573 and 31003A_175776) and the Novartis Research Foundation.

AUTHOR CONTRIBUTIONS

U.M., D.K., N.V., S.J.B.H., V.C., and T.D.M. carried out the experiments and analysis. H.K. carried out FACS analysis. N.A.M. prepared *EnvA-Rabies-ΔG-mCherry* virus. S.D. generated transgenic mouse lines. D.S., M.S., and S.A. generated the $Tau^{lsl\text{-}RabiesG}$ mouse line. C.F.K. established the trans-synaptic virus tracing approach. F.M.R. supervised the project and contributed to designing experiments and data analysis. F.M.R., U.M., and D.K. wrote the manuscript. All authors commented on the manuscript.

DECLARATION OF INTERESTS

The authors declare no competing interests.

Received: July 17, 2019
Revised: March 18, 2020
Accepted: May 21, 2020
Published: June 16, 2020

REFERENCES

Agger, K., Cloos, P.A., Christensen, J., Pasini, D., Rose, S., Rappsilber, J., Issaeva, I., Canaani, E., Salcini, A.E., and Helin, K. (2007). UTX and JMJD3 are

histone H3K27 demethylases involved in HOX gene regulation and development. Nature *449*, 731–734.

Allen, G.I., and Tsukahara, N. (1974). Cerebrocerebellar communication systems. Physiol. Rev. *54*, 957–1006.

Altman, J., and Bayer, S.A. (1987). Development of the precerebellar nuclei in the rat: IV. The anterior precerebellar extramural migratory stream and the nucleus reticularis tegmenti pontis and the basal pontine gray. J. Comp. Neurol. *257*, 529–552.

Baek, M., Pivetta, C., Liu, J.P., Arber, S., and Dasen, J.S. (2017). Columnar-Intrinsic Cues Shape Premotor Input Specificity in Locomotor Circuits. Cell Rep. *21*, 867–877.

Bechara, A., Laumonnerie, C., Vilain, N., Kratochwil, C.F., Cankovic, V., Maiorano, N.A., Kirschmann, M.A., Ducret, S., and Rijli, F.M. (2015). Hoxa2 Selects Barrelette Neuron Identity and Connectivity in the Mouse Somatosensory Brainstem. Cell Rep. *13*, 783–797.

Beier, K.T., Samson, M.E., Matsuda, T., and Cepko, C.L. (2011). Conditional expression of the TVA receptor allows clonal analysis of descendents from Cre-expressing progenitor cells. Dev. Biol. *353*, 309–320.

Bikoff, J.B., Gabitto, M.I., Rivard, A.F., Drobac, E., Machado, T.A., Miri, A., Brenner-Morton, S., Famojure, E., Diaz, C., Alvarez, F.J., et al. (2016). Spinal Inhibitory Interneuron Diversity Delineates Variant Motor Microcircuits. Cell *165*, 207–219.

Brodal, P. (1968). The corticopontine projection in the cat. I. Demonstration of a somatotopically organized projection from the primary sensorimotor cortex. Exp. Brain Res. *5*, 210–234.

Bulfone, A., Menguzzato, E., Broccoli, V., Marchitiello, A., Gattuso, C., Mariani, M., Consalez, G.G., Martinez, S., Ballabio, A., and Banfi, S. (2000). Barhl1, a gene belonging to a new subfamily of mammalian homeobox genes, is expressed in migrating neurons of the CNS. Hum. Mol. Genet. *9*, 1443–1452.

Burchfield, J.S., Li, Q., Wang, H.Y., and Wang, R.F. (2015). JMJD3 as an epigenetic regulator in development and disease. Int. J. Biochem. Cell Biol. *67*, 148–157.

Burgold, T., Voituron, N., Caganova, M., Tripathi, P.P., Menuet, C., Tusi, B.K., Spreafico, F., Bévengut, M., Gestreau, C., Buontempo, S., et al. (2012). The H3K27 demethylase JMJD3 is required for maintenance of the embryonic respiratory neuronal network, neonatal breathing, and survival. Cell Rep. *2*, 1244–1258.

Callaway, E.M., and Luo, L. (2015). Monosynaptic Circuit Tracing with Glycoprotein-Deleted Rabies Viruses. J. Neurosci. *35*, 8979–8985.

Cang, J., and Feldheim, D.A. (2013). Developmental mechanisms of topographic map formation and alignment. Annu. Rev. Neurosci. *36*, 51–77.

Chambeyron, S., and Bickmore, W.A. (2004). Chromatin decondensation and nuclear reorganization of the HoxB locus upon induction of transcription. Genes Dev. *18*, 1119–1130.

Chen, H., Zhang, H., Lee, J., Liang, X., Wu, X., Zhu, T., Lo, P.K., Zhang, X., and Sukumar, S. (2007). HOXA5 acts directly downstream of retinoic acid receptor beta and contributes to retinoic acid-induced apoptosis and growth inhibition. Cancer Res. *67*, 8007–8013.

D'Angelo, E., and Casali, S. (2013). Seeking a unified framework for cerebellar function and dysfunction: from circuit operations to cognition. Front. Neural Circuits *6*, 116.

Danielian, P.S., Muccino, D., Rowitch, D.H., Michael, S.K., and McMahon, A.P. (1998). Modification of gene activity in mouse embryos in utero by a tamoxifen-inducible form of Cre recombinase. Curr. Biol. *8*, 1323–1326.

Dasen, J.S., Liu, J.P., and Jessell, T.M. (2003). Motor neuron columnar fate imposed by sequential phases of Hox-c activity. Nature *425*, 926–933.

Davenne, M., Maconochie, M.K., Neun, R., Pattyn, A., Chambon, P., Krumlauf, R., and Rijli, F.M. (1999). Hoxa2 and Hoxb2 control dorsoventral patterns of neuronal development in the rostral hindbrain. Neuron *22*, 677–691.

De Kumar, B., Parrish, M.E., Slaughter, B.D., Unruh, J.R., Gogol, M., Seidel, C., Paulson, A., Li, H., Gaudenz, K., Peak, A., et al. (2015). Analysis of dynamic changes in retinoid-induced transcription and epigenetic profiles of murine Hox clusters in ES cells. Genome Res. *25*, 1229–1243.

De Santa, F., Totaro, M.G., Prosperini, E., Notarbartolo, S., Testa, G., and Natoli, G. (2007). The histone H3 lysine-27 demethylase Jmjd3 links inflammation to inhibition of polycomb-mediated gene silencing. Cell *130*, 1083–1094.

Di Bonito, M., Narita, Y., Avallone, B., Sequino, L., Mancuso, M., Andolfi, G., Franzè, A.M., Puelles, L., Rijli, F.M., and Studer, M. (2013). Assembly of the auditory circuitry by a Hox genetic network in the mouse brainstem. PLoS Genet. *9*, e1003249.

Di Meglio, T., Kratochwil, C.F., Vilain, N., Loche, A., Vitobello, A., Yonehara, K., Hrycaj, S.M., Roska, B., Peters, A.H., Eichmann, A., et al. (2013). Ezh2 orchestrates topographic migration and connectivity of mouse precerebellar neurons. Science *339*, 204–207.

Farago, A.F., Awatramani, R.B., and Dymecki, S.M. (2006). Assembly of the brainstem cochlear nuclear complex is revealed by intersectional and subtractive genetic fate maps. Neuron *50*, 205–218.

Ferraiuolo, M.A., Rousseau, M., Miyamoto, C., Shenker, S., Wang, X.Q., Nadler, M., Blanchette, M., and Dostie, J. (2010). The three-dimensional architecture of Hox cluster silencing. Nucleic Acids Res. *38*, 7472–7484.

Gaidatzis, D., Lerch, A., Hahne, F., and Stadler, M.B. (2015). QuasR: quantification and annotation of short reads in R. Bioinformatics *31*, 1130–1132.

Gavalas, A., Davenne, M., Lumsden, A., Chambon, P., and Rijli, F.M. (1997). Role of Hoxa-2 in axon pathfinding and rostral hindbrain patterning. Development *124*, 3693–3702.

Gavalas, A., Studer, M., Lumsden, A., Rijli, F.M., Krumlauf, R., and Chambon, P. (1998). Hoxa1 and Hoxb1 synergize in patterning the hindbrain, cranial nerves and second pharyngeal arch. Development *125*, 1123–1136.

Geisen, M.J., Di Meglio, T., Pasqualetti, M., Ducret, S., Brunet, J.F., Chedotal, A., and Rijli, F.M. (2008). Hox paralog group 2 genes control the migration of mouse pontine neurons through slit-robo signaling. PLoS Biol. *6*, e142.

Harkmark, W. (1954). Cell migrations from the rhombic lip to the inferior olive, the nucleus raphe and the pons; a morphological and experimental investigation on chick embryos. J. Comp. Neurol. *100*, 115–209.

Harris, J.A., Oh, S.W., and Zeng, H. (2012). Adeno-associated viral vectors for anterograde axonal tracing with fluorescent proteins in nontransgenic and cre driver mice. Curr. Protoc. Neurosci. *Chapter 1*, Unit 1, 1.20.1–1.20.18.

Helms, A.W., Abney, A.L., Ben-Arie, N., Zoghbi, H.Y., and Johnson, J.E. (2000). Autoregulation and multiple enhancers control Math1 expression in the developing nervous system. Development *127*, 1185–1196.

Hippenmeyer, S., Vrieseling, E., Sigrist, M., Portmann, T., Laengle, C., Ladle, D.R., and Arber, S. (2005). A developmental switch in the response of DRG neurons to ETS transcription factor signaling. PLoS Biol. *3*, e159.

Jessell, T.M., Sürmeli, G., and Kelly, J.S. (2011). Motor neurons and the sense of place. Neuron *72*, 419–424.

Jho, E.H., Zhang, T., Domon, C., Joo, C.K., Freund, J.N., and Costantini, F. (2002). Wnt/beta-catenin/Tcf signaling induces the transcription of Axin2, a negative regulator of the signaling pathway. Mol. Cell. Biol. *22*, 1172–1183.

Jiang, W., Wang, J., and Zhang, Y. (2013). Histone H3K27me3 demethylases KDM6A and KDM6B modulate definitive endoderm differentiation from human ESCs by regulating WNT signaling pathway. Cell Res. *23*, 122–130.

Karmakar, K., Narita, Y., Fadok, J., Ducret, S., Loche, A., Kitazawa, T., Genoud, C., Di Meglio, T., Thierry, R., Bacelo, J., et al. (2017). Hox2 Genes Are Required for Tonotopic Map Precision and Sound Discrimination in the Mouse Auditory Brainstem. Cell Rep. *18*, 185–197.

Kartikasari, A.E., Zhou, J.X., Kanji, M.S., Chan, D.N., Sinha, A., Grapin-Botton, A., Magnuson, M.A., Lowry, W.E., and Bhushan, A. (2013). The histone demethylase Jmjd3 sequentially associates with the transcription factors Tbx3 and Eomes to drive endoderm differentiation. EMBO J. *32*, 1393–1408.

Kashyap, V., Gudas, L.J., Brenet, F., Funk, P., Viale, A., and Scandura, J.M. (2011). Epigenomic reorganization of the clustered Hox genes in embryonic stem cells induced by retinoic acid. J. Biol. Chem. *286*, 3250–3260.

Kolmac, C.I., Power, B.D., and Mitrofanis, J. (1998). Patterns of connections between zona incerta and brainstem in rats. J. Comp. Neurol. *396*, 544–555.

Kosinski, R.J., Neafsey, E.J., and Castro, A.J. (1986). A comparative topographical analysis of dorsal column nuclear and cerebral cortical projections to the basilar pontine gray in rats. J. Comp. Neurol. *244*, 163–173.

Kwan, K.Y., Lam, M.M., Krsnik, Z., Kawasawa, Y.I., Lefebvre, V., and Sestan, N. (2008). SOX5 postmitotically regulates migration, postmigratory differentiation, and projections of subplate and deep-layer neocortical neurons. Proc. Natl. Acad. Sci. USA *105*, 16021–16026.

Lan, F., Bayliss, P.E., Rinn, J.L., Whetstine, J.R., Wang, J.K., Chen, S., Iwase, S., Alpatov, R., Issaeva, I., Canaani, E., et al. (2007). A histone H3 lysine 27 demethylase regulates animal posterior development. Nature *449*, 689–694.

Laumonnerie, C., Bechara, A., Vilain, N., Kurihara, Y., Kurihara, H., and Rijli, F.M. (2015). Facial whisker pattern is not sufficient to instruct a whisker-related topographic map in the mouse somatosensory brainstem. Development *142*, 3704–3712.

Lee, M.G., Villa, R., Trojer, P., Norman, J., Yan, K.P., Reinberg, D., Di Croce, L., and Shiekhattar, R. (2007). Demethylation of H3K27 regulates polycomb recruitment and H2A ubiquitination. Science *318*, 447–450.

Leergaard, T.B., and Bjaalie, J.G. (1995). Semi-automatic data acquisition for quantitative neuroanatomy. MicroTrace–computer programme for recording of the spatial distribution of neuronal populations. Neurosci. Res. *22*, 231–243.

Leergaard, T.B., and Bjaalie, J.G. (2007). Topography of the complete corticopontine projection: from experiments to principal Maps. Front. Neurosci. *1*, 211–223.

Leergaard, T.B., Lakke, E.A., and Bjaalie, J.G. (1995). Topographical organization in the early postnatal corticopontine projection: a carbocyanine dye and 3-D computer reconstruction study in the rat. J. Comp. Neurol. *361*, 77–94.

Leergaard, T.B., Alloway, K.D., Mutic, J.J., and Bjaalie, J.G. (2000a). Three-dimensional topography of corticopontine projections from rat barrel cortex: correlations with corticostriatal organization. J. Neurosci. *20*, 8474–8484.

Leergaard, T.B., Lyngstad, K.A., Thompson, J.H., Taeymans, S., Vos, B.P., De Schutter, E., Bower, J.M., and Bjaalie, J.G. (2000b). Rat somatosensory cerebropontocerebellar pathways: spatial relationships of the somatotopic map of the primary somatosensory cortex are preserved in a three-dimensional clustered pontine map. J. Comp. Neurol. *422*, 246–266.

Leergaard, T.B., Alloway, K.D., Pham, T.A., Bolstad, I., Hoffer, Z.S., Pettersen, C., and Bjaalie, J.G. (2004). Three-dimensional topography of corticopontine projections from rat sensorimotor cortex: comparisons with corticostriatal projections reveal diverse integrative organization. J. Comp. Neurol. *478*, 306–322.

Lein, E.S., Hawrylycz, M.J., Ao, N., Ayres, M., Bensinger, A., Bernard, A., Boe, A.F., Boguski, M.S., Brockway, K.S., Byrnes, E.J., et al. (2007). Genome-wide atlas of gene expression in the adult mouse brain. Nature *445*, 168–176.

Levine, A.J., Lewallen, K.A., and Pfaff, S.L. (2012). Spatial organization of cortical and spinal neurons controlling motor behavior. Curr. Opin. Neurobiol. *22*, 812–821.

Lin, C., Garrett, A.S., De Kumar, B., Smith, E.R., Gogol, M., Seidel, C., Krumlauf, R., and Shilatifard, A. (2011). Dynamic transcriptional events in embryonic stem cells mediated by the super elongation complex (SEC). Genes Dev. *25*, 1486–1498.

Liu, P., Jenkins, N.A., and Copeland, N.G. (2003). A highly efficient recombineering-based method for generating conditional knockout mutations. Genome Res. *13*, 476–484.

Madisen, L., Zwingman, T.A., Sunkin, S.M., Oh, S.W., Zariwala, H.A., Gu, H., Ng, L.L., Palmiter, R.D., Hawrylycz, M.J., Jones, A.R., et al. (2010). A robust and high-throughput Cre reporting and characterization system for the whole mouse brain. Nat. Neurosci. *13*, 133–140.

Mahony, S., Mazzoni, E.O., McCuine, S., Young, R.A., Wichterle, H., and Gifford, D.K. (2011). Ligand-dependent dynamics of retinoic acid receptor binding during early neurogenesis. Genome Biol. *12*, R2.

Margueron, R., and Reinberg, D. (2011). The Polycomb complex PRC2 and its mark in life. Nature *469*, 343–349.

Matsuda, T., and Cepko, C.L. (2007). Controlled expression of transgenes introduced by in vivo electroporation. Proc. Natl. Acad. Sci. USA *104*, 1027–1032.

Mazzoni, E.O., Mahony, S., Peljto, M., Patel, T., Thornton, S.R., McCuine, S., Reeder, C., Boyer, L.A., Young, R.A., Gifford, D.K., and Wichterle, H. (2013). Saltatory remodeling of Hox chromatin in response to rostrocaudal patterning signals. Nat. Neurosci. *16*, 1191–1198.

McIntyre, D.C., Rakshit, S., Yallowitz, A.R., Loken, L., Jeannotte, L., Capecchi, M.R., and Wellik, D.M. (2007). Hox patterning of the vertebrate rib cage. Development *134*, 2981–2989.

Mihailoff, G.A., Burne, R.A., and Woodward, D.J. (1978). Projections of the sensorimotor cortex to the basilar pontine nuclei in the rat: an autoradiographic study. Brain Res. *145*, 347–354.

Mihailoff, G.A., Adams, C.E., and Woodward, D.J. (1984). An autoradiographic study of the postnatal development of sensorimotor and visual components of the corticopontine system. J. Comp. Neurol. *222*, 116–127.

Mihailoff, G.A., Kosinski, R.J., Azizi, S.A., and Border, B.G. (1989). Survey of noncortical afferent projections to the basilar pontine nuclei: a retrograde tracing study in the rat. J. Comp. Neurol. *282*, 617–643.

Moreno-Juan, V., Filipchuk, A., Antón-Bolaños, N., Mezzera, C., Gezelius, H., Andrés, B., Rodríguez-Malmierca, L., Susín, R., Schaad, O., Iwasato, T., et al. (2017). Prenatal thalamic waves regulate cortical area size prior to sensory processing. Nat. Commun. *8*, 14172.

Narita, Y., and Rijli, F.M. (2009). Hox genes in neural patterning and circuit formation in the mouse hindbrain. Curr. Top. Dev. Biol. *88*, 139–167.

Niederreither, K., and Dollé, P. (2008). Retinoic acid in development: towards an integrated view. Nat. Rev. Genet. *9*, 541–553.

Noordermeer, D., Leleu, M., Splinter, E., Rougemont, J., De Laat, W., and Duboule, D. (2011). The dynamic architecture of Hox gene clusters. Science *334*, 222–225.

O'Leary, D.D., and Terashima, T. (1988). Cortical axons branch to multiple subcortical targets by interstitial axon budding: implications for target recognition and "waiting periods". Neuron *1*, 901–910.

O'Leary, D.D., Heffner, C.D., Kutka, L., Lopez-Mascaraque, L., Missias, A., and Reinoso, B.S. (1991). A target-derived chemoattractant controls the development of the corticopontine projection by a novel mechanism of axon targeting. Dev. Suppl. *1991* (*Suppl. 2*), 123–130.

Okada, T., Keino-Masu, K., and Masu, M. (2007). Migration and nucleogenesis of mouse precerebellar neurons visualized by in utero electroporation of a green fluorescent protein gene. Neurosci. Res. *57*, 40–49.

Ordóñez-Morán, P., Dafflon, C., Imajo, M., Nishida, E., and Huelsken, J. (2015). HOXA5 Counteracts Stem Cell Traits by Inhibiting Wnt Signaling in Colorectal Cancer. Cancer Cell *28*, 815–829.

Osakada, F., and Callaway, E.M. (2013). Design and generation of recombinant rabies virus vectors. Nat. Protoc. *8*, 1583–1601.

Oury, F., Murakami, Y., Renaud, J.S., Pasqualetti, M., Charnay, P., Ren, S.Y., and Rijli, F.M. (2006). Hoxa2- and rhombomere-dependent development of the mouse facial somatosensory map. Science *313*, 1408–1413.

Panto, M.R., Cicirata, F., Angaut, P., Parenti, R., and Serapide, F. (1995). The projection from the primary motor and somatic sensory cortex to the basilar pontine nuclei. A detailed electrophysiological and anatomical study in the rat. J. Hirnforsch. *36*, 7–19.

Park, D.H., Hong, S.J., Salinas, R.D., Liu, S.J., Sun, S.W., Sgualdino, J., Testa, G., Matzuk, M.M., Iwamori, N., and Lim, D.A. (2014). Activation of neuronal gene expression by the JMJD3 demethylase is required for postnatal and adult brain neurogenesis. Cell Rep. *8*, 1290–1299.

Philippidou, P., and Dasen, J.S. (2013). Hox genes: choreographers in neural development, architects of circuit organization. Neuron *80*, 12–34.

Pierce, E.T. (1973). Time of origin of neurons in the brain stem of the mouse. Prog. Brain Res. *40*, 53–65.

Puschendorf, M., Terranova, R., Boutsma, E., Mao, X., Isono, K., Brykczynska, U., Kolb, C., Otte, A.P., Koseki, H., Orkin, S.H., et al. (2008). PRC1 and Suv39h

specify parental asymmetry at constitutive heterochromatin in early mouse embryos. Nat. Genet. *40*, 411–420.

Ramadoss, S., Chen, X., and Wang, C.Y. (2012). Histone demethylase KDM6B promotes epithelial-mesenchymal transition. J. Biol. Chem. *287*, 44508–44517.

Rodriguez, C.I., and Dymecki, S.M. (2000). Origin of the precerebellar system. Neuron *27*, 475–486.

Rodríguez, C.I., Buchholz, F., Galloway, J., Sequerra, R., Kasper, J., Ayala, R., Stewart, A.F., and Dymecki, S.M. (2000). High-efficiency deleter mice show that FLPe is an alternative to Cre-loxP. Nat. Genet. *25*, 139–140.

Rossant, J., Zirngibl, R., Cado, D., Shago, M., and Giguère, V. (1991). Expression of a retinoic acid response element-hsplacZ transgene defines specific domains of transcriptional activity during mouse embryogenesis. Genes Dev. *5*, 1333–1344.

Rousseau, M., Crutchley, J.L., Miura, H., Suderman, M., Blanchette, M., and Dostie, J. (2014). Hox in motion: tracking HoxA cluster conformation during differentiation. Nucleic Acids Res. *42*, 1524–1540.

Santagati, F., Minoux, M., Ren, S.Y., and Rijli, F.M. (2005). Temporal requirement of Hoxa2 in cranial neural crest skeletal morphogenesis. Development *132*, 4927–4936.

Schwarz, C., and Thier, P. (1995). Modular organization of the pontine nuclei: dendritic fields of identified pontine projection neurons in the rat respect the borders of cortical afferent fields. J. Neurosci. *15*, 3475–3489.

Schwarz, C., Horowski, A., Möck, M., and Thier, P. (2005). Organization of tectopontine terminals within the pontine nuclei of the rat and their spatial relationship to terminals from the visual and somatosensory cortex. J. Comp. Neurol. *484*, 283–298.

Seidler, B., Schmidt, A., Mayr, U., Nakhai, H., Schmid, R.M., Schneider, G., and Saur, D. (2008). A Cre-loxP-based mouse model for conditional somatic gene expression and knockdown in vivo by using avian retroviral vectors. Proc. Natl. Acad. Sci. USA *105*, 10137–10142.

Shinohara, M., Zhu, Y., and Murakami, F. (2013). Four-dimensional analysis of nucleogenesis of the pontine nucleus in the hindbrain. J. Comp. Neurol. *521*, 3340–3357.

Stanfield, B.B., and O'Leary, D.D. (1985). The transient corticospinal projection from the occipital cortex during the postnatal development of the rat. J. Comp. Neurol. *238*, 236–248.

Studer, M., Lumsden, A., Ariza-McNaughton, L., Bradley, A., and Krumlauf, R. (1996). Altered segmental identity and abnormal migration of motor neurons in mice lacking Hoxb-1. Nature *384*, 630–634.

Sürmeli, G., Akay, T., Ippolito, G.C., Tucker, P.W., and Jessell, T.M. (2011). Patterns of spinal sensory-motor connectivity prescribed by a dorsoventral positional template. Cell *147*, 653–665.

Swenson, R.S., Kosinski, R.J., and Castro, A.J. (1984). Topography of spinal, dorsal column nuclear, and spinal trigeminal projections to the pontine gray in rats. J. Comp. Neurol. *222*, 301–311.

Tan, K., and Le Douarin, N.M. (1991). Development of the nuclei and cell migration in the medulla oblongata. Application of the quail-chick chimera system. Anat. Embryol. (Berl.) *183*, 321–343.

Taniguchi, H., Kawauchi, D., Nishida, K., and Murakami, F. (2006). Classic cadherins regulate tangential migration of precerebellar neurons in the caudal hindbrain. Development *133*, 1923–1931.

Terenzi, M.G., Zagon, A., and Roberts, M.H. (1995). Efferent connections from the anterior pretectal nucleus to the diencephalon and mesencephalon in the rat. Brain Res. *701*, 183–191.

Testa, G., Schaft, J., van der Hoeven, F., Glaser, S., Anastassiadis, K., Zhang, Y., Hermann, T., Stremmel, W., and Stewart, A.F. (2004). A reliable lacZ expression reporter cassette for multipurpose, knockout-first alleles. Genesis *38*, 151–158.

Tripodi, M., Stepien, A.E., and Arber, S. (2011). Motor antagonism exposed by spatial segregation and timing of neurogenesis. Nature *479*, 61–66.

Tümpel, S., Wiedemann, L.M., and Krumlauf, R. (2009). Hox genes and segmentation of the vertebrate hindbrain. Curr. Top. Dev. Biol. *88*, 103–137.

van de Werken, H.J., Landan, G., Holwerda, S.J., Hoichman, M., Klous, P., Chachik, R., Splinter, E., Valdes-Quezada, C., Oz, Y., Bouwman, B.A., et al. (2012). Robust 4C-seq data analysis to screen for regulatory DNA interactions. Nat. Methods *9*, 969–972.

Wang, V.Y., Rose, M.F., and Zoghbi, H.Y. (2005). Math1 expression redefines the rhombic lip derivatives and reveals novel lineages within the brainstem and cerebellum. Neuron *48*, 31–43.

Warming, S., Costantino, N., Court, D.L., Jenkins, N.A., and Copeland, N.G. (2005). Simple and highly efficient BAC recombineering using galK selection. Nucleic Acids Res. *33*, e36.

Wickersham, I.R., Lyon, D.C., Barnard, R.J., Mori, T., Finke, S., Conzelmann, K.K., Young, J.A., and Callaway, E.M. (2007). Monosynaptic restriction of transsynaptic tracing from single, genetically targeted neurons. Neuron *53*, 639–647.

Wickersham, I.R., Sullivan, H.A., and Seung, H.S. (2010). Production of glycoprotein-deleted rabies viruses for monosynaptic tracing and high-level gene expression in neurons. Nat. Protoc. *5*, 595–606.

Wiesendanger, R., and Wiesendanger, M. (1982). The corticopontine system in the rat. I. Mapping of corticopontine neurons. J. Comp. Neurol. *208*, 215–226.

Zhang, J., Smith, D., Yamamoto, M., Ma, L., and McCaffery, P. (2003). The meninges is a source of retinoic acid for the late-developing hindbrain. J. Neurosci. *23*, 7610–7620.

STAR★METHODS

KEY RESOURCES TABLE

REAGENT or RESOURCE	SOURCE	IDENTIFIER
Antibodies		
Rabbit anti-Pax6	Millipore	Cat# AB2237, RRID:AB_1587367
Rabbit anti-Hoxa5	Sigma	Cat# HPA029319, RRID:AB_10601430
Rabbit anti-RFP	Rockland	Cat# 600-401-379, RRID:AB_2209751
Rabbit anti-Barhl1	Sigma	Cat# HPA004809, RRID:AB_1078266
Rat anti-Hoxb4	DSHB	Cat# I12 anti-Hoxb4, RRID:AB_2119288
Chicken anti-GFP	Thermo Fisher Scientific	Cat# A10262, RRID:AB_2534023
Rat anti-Ki67	e-Biosciences	Cat# 14-5689-82, RRID:AB_10854564
Chicken anti-mcherry	Novus Biologicals	Cat# NBP2-25158, RRID:AB_2636881
Rabbit anti-RAR for ChIP	Santa Cruz	Cat# sc-773, RRID:AB_2175398
Rabbit anti-Jmjd3 for ChIP	Abcam	Cat# ab38113, RRID:AB_943898
Bacterial and Virus Strains		
EnvA-Rabies-ΔG-mCherry	Edward Callaway	N/A
SAD-ΔG-mCherry	Edward Callaway	N/A
AAV1.hSyn.GFP.WPRE.bGH	Penn Vectors	AV-1-PV1696
pCX-eGFP	Okada et al., 2007	N/A
pCX-rabies-glycoprotein-WPRE	Filippo Rijli	N/A
pAAV-EF1a-TVA-WPRE	Botond Roska	N/A
pCAG-mGFP-2a-Cyp26b1	Filippo Rijli	N/A
pCAG-Cre	Filippo Rijli	N/A
pCAG-ERT2CreERT2	Matsuda and Cepko, 2007	Addgene Plasmid Cat# 13777, RRID:Addgene_13777
pCAG-Unc5b	Di Meglio et al., 2013	N/A
pKS-β-globin-lacZ	Studer et al., 1996	N/A
pR26-CAG-lsl-Kir	Guillermina Lopez-Bendito	N/A
plasmid pN21-Cre	Di Meglio et al., 2013	N/A
plasmid PL451	Liu et al., 2003	N/A
BAC clone RP23-401D9	BACPAC Resources Center	RP23-401D9
Chemicals, Peptides, and Recombinant Proteins		
Tamoxifen	Sigma	Cat# T5648-5G
4-Hydroxy-Tamoxifen	Sigma	Cat# H6278-50MG
Retinoic Acid	Sigma	Cat# R2625
Papain	Roche	Cat# 000000010108014001
Sucrose	Sigma-Aldrich	Cat# 84100
Gelatin	Sigma-Aldrich	Cat# G2500
Agarose	Promega	Cat# V3125
Corn oil	Aldo	Cat# N/A
Exonuclease I	NEB	Cat# M0293S
DNA Suspension Buffer	TEKnova,	Cat# T0221
Trypsin	Sigma-Aldrich	Cat# T5266
Collagenase Type II	GIBCO	Cat# 17101-015
Protease Inhibitors	Roche	Cat# 000000011836170001
Proteinase-K	Sigma-Aldrich	Cat# P8044
Paraformaldehyde	Sigma	Cat# 158127-500 g

(*Continued on next page*)

Continued

REAGENT or RESOURCE	SOURCE	IDENTIFIER
Glutaraldehyde solution (25%)	Sigma	Cat# G-5882-10X1ml
20% SDS Solution	Sigma	Cat# 05030-1L-F
t-RNA from Baker's yeast	Roche	Cat# 10109509001
Levamisole Hydrochloride	Sigma	Cat# L9756-10 g
Heparin Sodium Salt	Applichem	Cat# A3004,0500
Formamide	Fluka	Cat# 47670-1L-F
CHAPS	Sigma	Cat# C3023-5G
Tween-20	Sigma	Cat# P1379-250ml
Blocking Reagent	Roche	Cat# 11096176001
DIG RNA labeling mix	Roche	Cat# 11277073910
Anti DIG-AP (Fab Fragment)	Roche	Cat# 11093274910
RNase A	Roche	Cat# 10109169001
NBT (4-Nitro blue tetrazolium chloride)	Roche	Cat# 11383213001
BCIP	Roche	Cat# 11383221001
EDTA	Sigma	Cat# E5134-1KG
RNasin Plus RNase Inhibitor	Promega	Cat# N2615
T3 RNA polymerase	Promega	Cat# P2083
T7 RNA polymerase	Promega	Cat# P2075
SP6 RNA polymerase	Promega	Cat# P1085
DIG RNA labeling mix	Roche	Cat# 11277073910
Critical Commercial Assays		
RNAScope Multiplex Fluorescent Kit	Bio-techne	Cat# 320850
RNAScope Universal Pretreatment Kit	Bio-techne	Cat# 322380
CellsDirect One-Step qPCR Kit	Invitrogen	Cat# 11753-100
Mini-elute PCR purification Kit	QIAGEN	Cat# ID:28004
EndoFree Plasmid Maxi kit	QIAGEN	Cat# ID:12362
PicoPure RNA isolation Kit	Applied Biosystems	Cat# 15295033
Ovation RNA Amplification System V2	NuGEN	Cat# 3100-60
RNA Sequencing TotalScript RNA-seq Kit	Epicenter	Cat# TSRNA1296
TOPO TA Cloning Kit, Dual Promoter	Invitrogen	Cat# K4600-40
Deposited Data		
Allen Developing Mouse Brain Atlas	Allen Institute for Brain Science	http://developingmouse.brain-map.org
4C-Sequencing	This paper	GEO: GSE72709
RNA-Sequencing	This paper	GEO:GSE72710
Experimental Models: Cell Lines		
B19G2	Edward Callaway	N/A
BHK-EnvA2	Edward Callaway	N/A
ES Cell clone: EPD0330_7_F03, Kdm6b$^{tm1(KOMP)Wtsi}$	KOMP (https://www.komp.org)	EPD0330_7_F03
E14 ES Cell line	FMI Transgenic Mouse Facility	N/A
Experimental Models: Organisms/Strains		
Mouse: Atoh1(45)::Cre	This paper	N/A
Mouse: Kdm6b/Jmjd3 Knock-In line	This paper	N/A
Mouse: ROSA26::(lox-stop-lox)Hoxa5-IRES-GFP BAC transgenic line	This paper	N/A
Mouse: ROSA26::(lox-stop-lox)Hoxa5-IRES-GFP Knock-In line	This paper	N/A
Mouse: Tau::(lox-stop-lox)Rabies-glycoprotein-IRES-nls-LacZ	This paper	N/A

(*Continued on next page*)

Continued

REAGENT or RESOURCE	SOURCE	IDENTIFIER
Mouse: Hoxa5::Cre knock-in line	This paper	N/A
Mouse: RARE::LacZ	Rossant et al., 1991	RRID:IMSR_JAX:008477
Mouse: ACTB::Flip	Rodríguez et al., 2000	N/A
Mouse: Wnt1::Cre	Danielian et al., 1998	RRID:IMSR_JAX:003829
Mouse: r5-6::Cre	Di Meglio et al., 2013	N/A
Mouse: Hoxa5::Cre BAC Transgenic	Di Meglio et al., 2013	N/A
Mouse: MafB::CreERT2	Di Meglio et al., 2013	N/A
Mouse: Ezh2$^{fl/fl}$	Puschendorf et al., 2008	N/A
ROSA::(lox-stop-lox)TVA-IRES-LacZ	Seidler et al., 2008	N/A
ROSA::(lox-stop-lox)tdTomato	Madisen et al., 2010	RRID:IMSR_JAX:007905
Oligonucleotides		
See Table S2 for oligonucleotide information		N/A
Recombinant DNA		
Hoxa2 riboprobe plasmid	Filippo Rijli	N/A
Hoxa3 riboprobe plasmid	Geisen et al., 2008	N/A
Hoxb4 riboprobe plasmid	Geisen et al., 2008	N/A
Hoxa5 riboprobe plasmid	McIntyre et al., 2007	N/A
Hoxb5 riboprobe plasmid	Geisen et al., 2008	N/A
Barhl1 riboprobe plasmid	Geisen et al., 2008	N/A
Wnt1 riboprobe plasmid	Di Meglio et al., 2013	N/A
Axin2 riboprobe plasmid	Paola Bovolenta	N/A
Ezh2 riboprobe plasmid	Filippo Rijli	N/A
Slit3 riboprobe plasmid	Alain Chédotal	N/A
Raldh2 riboprobe plasmid	Pascal Dollé	N/A
Cyp26b1 riboprobe plasmid	Filippo Rijli	N/A
Crabp1 riboprobe plasmid	Filippo Rijli	N/A
Nrp2 riboprobe plasmid	Alain Chédotal	N/A
Software and Algorithms		
QuasR Package	Bioconductor	https://www.bioconductor.org/packages/release/bioc/html/QuasR.html
BioStrings Package	Bioconductor	https://bioconductor.org/packages/release/bioc/html/Biostrings.html
GO Enrichment Analysis too	PANTHER	http://geneontology.org/docs/go-enrichment-analysis/
JASPAR2018	N/A	http://jaspar2018.genereg.net
Zen	Zeiss	https://www.zeiss.com/microscopy/us/products/microscope-software/zen.html
ImageJ	NIH	https://imagej.nih.gov/ij/download.html
IMARIS	BITPLANE	N/A
GraphPad Prism	GraphPad Software	https://www.graphpad.com/scientific-software/prism/
Other		
Disposable plastic feeding tubes for oral gavage	Instech laboratories Inc. USA	Cat# FTP-20-38-50

RESOURCE AVAILABILITY

Lead Contact

Further information and requests for resources and reagents should be directed to and will be fulfilled by the Lead Contact, Filippo M. Rijli (filippo.rijli@fmi.ch).

Materials Availability

Reagents generated in this study will be made available on request upon completion of a Material Transfer Agreement.

Data and Code Availability

4C seq and RNA seq data and analysis was deposited into the GEO repository under accession numbers GEO: GSE72709 and GEO: GSE72710, respectively.

EXPERIMENTAL MODEL AND SUBJECT DETAILS

Mouse Genetics

All animal procedures were performed in accordance with institutional animal care guidelines and were approved by the Veterinary Department of the Kanton Basel-Stadt. *In vivo* experiments were approved under permits 2363, 2708, and 2670. Sex of embryos and fetuses was not determined. For postnatal experiments, both sexes were used interchangeably. No phenotypic differences between male and female animals are expected, but were not formally tested. Age of each specimen, embryonic or postnatal, has been reported in figure legends and wherever appropriate in the Results section.

Previously available mouse lines used were: *RARE::lacZ* (Rossant et al., 1991), *ACTB::Flip* (Rodríguez et al., 2000), *Wnt1::Cre* (Danielian et al., 1998), *r5-6::Cre*, *Hoxa5::Cre*, *MafB::CreERT2* (Di Meglio et al., 2013), *Ezh2*$^{fl/fl}$ (Puschendorf et al., 2008), and *ROSA26::(lox-stop-lox)TVA-IRES-lacZ* (Seidler et al., 2008) lines were as described. *ROSA26::(lox-stop-lox)tdTomato* (Madisen et al., 2010) mice were obtained from The Jackson Laboratory, USA (JAX stock #007905). Other mouse lines generated for this study are described below.

Generation of the Atoh1(45)::Cre line

The original goal was to create a *Atoh1::CreERT2* line. Due to Cre activity in absence of tamoxifen for one of the founder (#45), this line was used as a normal Cre line and renamed *Atoh1(45)::Cre*. In these transgenic mice, the *Cre* is driven by a 1.7 kb enhancer of *Atoh1* (Helms et al., 2000). The enhancer was subcloned into the vector pKS-β-globin-CreERT2-SV40pA, created by replacing the *lacZ* gene of the pKS-β-globin-lacZ vector (BGZ40) (Studer et al., 1996) with a CreERT2 cassette (Santagati et al., 2005) using homologous recombination. The enhancer was amplified by PCR from genomic DNA using the following primers: 5′AGT TGT GCC TGT CTA AGG TC 3′ and 5′ATC TAC TAG TGC TCT GGC TTC TGT AAA CTC 3′. The PCR band was purified and inserted 5′ of the β-globin promoter using restriction sites SacII and SpeI, thus generating a construct consisting of the enhancer, a β-globin minimal promoter and CreERT2 encoding sequence. The construct was linearized, purified and microinjected into the pronuclei of mouse zygotes. Founders were identified by PCR (907bp fragment) using the primers described in the Key Resources Table.

Generation of the Jmjd3 knock-in line

We generated a null allele of the H3K27 demethylase *Kdm6b*/*Jmjd3* by using a targeting construct which replaced most of the gene with a frt-flanked cassette including *lacZ* (referred to as *Jmjd3*$^{lacZ/lacZ}$ or *Jmjd3*$^{-/-}$ after Flp-mediated excision of the targeting cassette). The knock-in mouse strain *Jmjd3*^{lacZ} was created from the ES cell clone (EPD0330_7_F03, Kdm6b$^{tm1(KOMP)Wtsi}$) obtained from the NCRR-NIH supported KOMP Repository (https://www.komp.org) and generated by the CSD consortium for the NIH funded Knockout Mouse Project (KOMP) (Testa et al., 2004). The ES cells were aggregated with morula-stage embryos obtained from inbred (C57BL/6 x DBA/2) F1 mice. Germline transmission of the *Kdm6b*$^{tm1(KOMP)Wtsi}$ allele was obtained and heterozygous mice were viable and fertile. The mice were genotyped by PCR (359bp wild-type and 572bp mutant fragments) with the primers described in the Key Resources Table. The in-frame *lacZ* expression cassette was flanked by two *frt* sites, which allowed Flp-mediated removal.

Generation of the ROSA26::(lox-stop-lox)Hoxa5-IRES-GFP BAC transgenic line

The generation of the conditional *Hoxa5* overexpression BAC transgenic line was a two-step process. First we generated a BAC *ROSA26::(lox-stop-lox)galK-IRES-GFP*, used it as an entry for further constructs and allowing us the introduction of different cDNAs between the lox-stop-lox sequence and the IRES-GFP by using BAC recombineering and galK negative selection (Warming et al., 2005). Then we used this strategy to replace the *galK* gene by a codon optimized DNA sequence encoding for the Hoxa5 protein. The original BAC clone RP23-401D9 containing the ROSA26 locus was obtained from BACPAC Resources Center (Children's Hospital Oakland Research Institute, Oakland, Calif., USA) and was used as a template for bacterial recombination. To prevent any further interactions, the LoxP511 and the LoxP sites located in the backbone vector of this BAC were removed respectively by recombination of an ampicillin resistance gene and by using the galK positive/negative selection (Warming et al., 2005). The final BAC *ROSA26::(lox-stop-lox)Hoxa5-IRES-GFP* (consisting of a splice acceptor, a lox-PGK-Neo-3xpA(stop)-lox cassette, a codon optimized *Hoxa5*, an IRES-GFP-pA) and all the intermediate constructs were tested by PCR, restriction enzyme digestion and sequencing for correct recombination and removals of the lox/galK sequences. The purified BAC was linearized by PI-SceI digestion prior to microinjection into pronuclei of mouse zygotes. Founders were identified by PCR (220bp fragment) using the primers described in the Key Resources Table.

Generation of the ROSA26::CAG(lox-stop-lox)3xFlag-Hoxa5-IRES-GFP knock-in line

The conditional Hoxa5 overexpression mouse line was generated by homologous recombination in the ROSA26 locus using the targeting vector *pR26-CAG-lsl-3xflagHoxa5-IRES-GFP*, consisting of a CAG promoter, a lox-stop-lox cassette, a codon optimized

Hoxa5 tagged with a 3xFlag, an IRES-GFP, a WPRE element, a bGH poly(A) and a PGK-Neo cassette. To generate this vector, we used the vector *pR26-CAG-lsl-Kir* (kind gift from Guillermina López-Bendito; Moreno-Juan et al., 2017), in which we replaced the insert located between the two FseI restriction sites by the cassette 3xflagHoxa5-IRES-GFP (PCR amplified from the BAC *ROSA26::(lox-stop-lox)Hoxa5-IRES-GFP* and cloned into the TOPO vector pCRII (Invitrogen) with insertion of a 3xFlag tag). The final targeting vector *pR26-CAG-lsl-3xflagHoxa5-IRES-GFP* was linearized with PvuI and electroporated into the E14 ES cell line. The positive ES cell clones selected by G418 resistance and screened by PCR were aggregated with morula-stage embryos obtained from inbred (C57BL/6 x DBA/2) F1 mice. Germline transmission of the *ROSA26::CAG(lox-stop-lox)3xFlag-Hoxa5-IRES-GFP* allele was obtained. Heterozygous and homozygous mice were viable and fertile. The mice were genotyped by PCR (603-bp wild-type and 325-bp mutant fragments) with the primers described in the Key Resources Table.

Generation of the Tau::(lox-stop-lox)Rabies-glycoprotein-IRES-nls-lacZ

The *Tau::(lox-stop-lox)Rabies-glycoprotein-IRES-nls-lacZ* mouse line was generated by inserting a cassette encoding (lox-stop-lox) Rabies-glycoprotein-IRES-nls-lacZ into exon 2 of the Tau locus using a strategy described previously (Hippenmeyer et al., 2005).

Generation of Hoxa5::Cre knock-in line

We generated a targeting construct *pHoxa5-Cre-FRT-Neo-FRT* consisting of a Cre cassette and a SV40 poly A signal derived from the plasmid pN21-Cre (Di Meglio et al., 2013) followed by cassette *FRT–PGK–NeobpA–FRT* from the plasmid PL451 (Liu et al., 2003), flanked by 5′ and 3′ homology arms corresponding to 1125 bases upstream and 1619 bases starting 45 bases downstream of the *Hoxa5* ATG codon respectively. This construct, initially prepared for homologous recombination in mouse embryonic stem cells, was used to produce a linear double stranded (ds) DNA template for mouse zygote injection in combination with the CRISPR/Cas9 system. The targeting construct was digested by the restriction enzyme PspOMI and gel purified to obtain a linear 5,5 kb dsDNA template composed by the cassette Cre-SV40polyA-FRT-Neo-FRT flanked by 5′ and 3′ homology arms of 0.98 kb and 1.5 kb respectively.

We designed a single guide (sg)RNA, produced by Integrated DNA Technologies (IDT), to target *Hoxa5* at the following protospacer sequence: TTTTGCGGTCGCTATCCAAA.

For zygote injection, sgRNA (50 ng/μl), cas9 mRNA (100 ng/μl) and the linear dsDNA template (45 ng/μl) were mixed in 0.1 TE buffer (10 mM Tris-HCl pH 7.4, 0.1 mM EDTA pH 8.0) and microinjected into the pronuclei of B6CF2 mouse zygotes. Knock-in founder was identified by PCR and Southern-Blot. Germline transmission of the *Hoxa5::Cre(FRT-neo-FRT)* allele was confirmed and *in vivo* Flp-mediated excision of the PGK-*neo* cassette was obtained by mating the *Hoxa5::Cre(FRT-neo-FRT)* mice to the ACTB:FLPe deleter. The mice were genotyped by PCR (317bp wild-type and 581bp mutant fragments) with the primers described in the Key Resources Table.

METHOD DETAILS

Tissue sectioning

Prenatal heads were collected, dissected if necessary, and fixed in 4% PFA diluted in 1xPBS from 30 minutes at room temperature to overnight at 4°C. Postnatal animals were perfused with 4% PFA diluted in 1xPBS for 10 minutes and post fixed in 4% PFA diluted in 1xPBS overnight at 4°C. For cryostat sections, tissues were cryoprotected in 20% sucrose/ 1xPBS and embedded in 7.5% gelatin/ 10% sucrose/ 1xPBS before being frozen at −80°C. Cryostat sections (25-30 μm) were cut (Microm HM560) in coronal and sagittal orientations. Vibratome sections (50-80 μm) were prepared from postnatal brains after embedding in 4% agarose/ 0.1 M phosphate buffer (pH7.4).

Immunohistochemistry

Immunohistochemistry was performed as described before (Geisen et al., 2008). Following antibodies were used: rabbit anti-Pax6 (1/1000), rabbit anti-Hoxa5 (1/100), rabbit anti-RFP (1/1000), rabbit anti-Barhl1 (1/200), rat anti-Hoxb4 (1/100), chicken anti-GFP (/500), Rat anti-Ki67 (1/250) and chicken anti-mcherry (1/500) followed by species-specific fluorochrome-coupled secondary antibody staining (Alexa Fluor 488, 546, or 647, 1/500). Nuclei were stained with DAPI (Invitrogen, 1/10000).

In Situ Hybridization

Simple and double *in situ* hybridizations were performed as described previously (Geisen et al., 2008). The following probes were used: *Barhl1, Wnt1, Axin2, Hoxa2, Hoxa3, Hoxb4, Hoxb5, Hoxa5, Ezh2, Cyp26b1, Raldh2, Nrp2, Slit3, SST, Calbindin1, Crabp1, and Lmo3*. β-Galactosidase staining were performed as described previously (Geisen et al., 2008).

RNA-FISH

Fluorescent *in situ* hybridization (FISH) were performed using the RNAscope Multiplex Fluorescent Kit according to the protocol described in Laumonnerie et al., 2015. Targeted sequences were: Mm-*Unc5b*-C1, nucleotides 3531 – 4791 of accession number NM_029770.2 and Mm-*Barhl1*-C3, nucleotide 821 – 2282 of accession number NM_019446.4. A probe against the gene encoding POL2RA, a protein expressed in mammalian cells, was used as positive control, and a probe against *Escherichia coli dapB* (not

expressed in mammalian cells) was used as a negative control (data not shown). Imaging was done on Nikon Ti2-E Eclipse spinning disk, image analysis was done using Fiji and IMARIS (Bitplane).

In vivo treatment

Retinoic acid (RA) was dissolved in DMSO and administered to pregnant mice by intraperitoneal injection (30mg/Kg at E11.5 or 60mg/kg at E9.5). Tamoxifen was dissolved in corn oil (10mg/ml stock solution) and was administered by oral gavage at E7.5 (1mg) to *Mafb::CreERT2* mice. For activation of Cre from *ERT2CreERT2* plasmid, 1mg of 4-Hydroxytamoxifen (4-OHT) (dissolved in 50μL Ethanol, diluted to 500μL with corn oil) was administered to pregnant mice orally at E18.5. For oral gavage, disposable plastic feeding tubes were used.

In utero electroporation

In utero electroporation was performed on embryos at E13.5 or E14.5 as described previously (Taniguchi et al., 2006). Plasmids used for electroporation were diluted to 1.5mg/ml in 1x phosphate buffer (PBS). Plasmids used in this study were as follows: *pCX-eGFP*, *pCX-rabies-glycoprotein-WPRE*, *pCAG-mGFP-2a-Cyp26b1*, *pAAV-EF1a-TVA-WPRE* (kind gift from Botond Roska), *pCAG-Cre*, *pCAG-ERT2CreERT2*, *pcDNA-Unc5b*

Fluorescent activated Cell Sorting (FACS)

Regions of interest were micro-dissected in 1xPBS at the desired stage and incubated for 5 – 10 minutes in activated dissociation solution (HBSS, 2.5mM Cystein, 0.5mM EDTA, 10mM HEPES, 1mg/ml Papain) at 37°C. Samples were rinsed five times in HBSS/ 10% FBS. Single cell suspension was achieved through mechanical dissociation of tissue with Pasteur pipettes. Fluorescent cells were collected by FACS (FACSCalibur, Becton Dickson) in appropriate solutions for further analysis.

Quantitative PCR (qPCR)

100 cells isolated by FACS were directly sorted into the reverse transcription (RT) buffer (1x CellsDirect One-Step qPCR Kit, Super-Script III RT Platinum Taq Mix, Primer mix (50nM final concentration)). RT was done for 15 minutes at 50°C followed by inactivation of the reverse transcriptase and activation of the Taq at 95°C for 2 minutes. 18 cycles (95°C 15 s, 60°C 4 minutes) of pre-amplification of specific targets was done on a standard thermal cycler. Unincorporated primers were removed by Exonuclease I treatment for 30 minutes at 37°C. The final product was diluted 10-fold with DNA Suspension Buffer. qPCR was carried out with StepOne Real Time PCR System (Applied Biosystems) with the primers described in the Key Resources Table. Calculations were done using the delta delta cycle threshold (ddCt) model using Ssu72 as endogenous control.

Chromatin immunoprecipitation (ChIP)

Micro-dissected tissue samples were dissociated to single cells. Cells were cross-linked for 15 min in 1% PFA/1xPBS solution and subsequently lysed in cell lysis buffer (5mM PIPES pH8.0, 85mM KCl, 0.5% NP40, and protease inhibitors) for 10 min on ice. Nuclei were spin down at 2500 g for 5 min at 4°C and finally lysed in nuclei lysis buffer (50mM Tris-HCl pH8.0, 10mM EDTA, 1% SDS and protease inhibitors). Following 15 min of lysis on a tube shaker at 4°C, samples were sonicated on Covaris and centrifuged at 22000 g for 15 min at 4°C. Chromatin preparation was diluted 10x with IP Dilution Buffer (0.01% SDS, 1.1% Triton X-100, 1.2mM EDTA, 16.7mM Tris-HCl pH8.0, 167 mM NaCl, and protease inhibitors) and used for IP. For IP, chromatin preparations were incubated overnight with primary antibodies on a tube roller at 4°C. 50 μL of protein G magnetic beads was added and the incubation continued for 2 h. Beads were washed 3 times with 1ml of 0.02% Tween20/TBS solution. Precipitated material was eluted twice for 15min with 100 μL of 1% SDS/ 100 mM sodium hydrogencarbonate (NaHCO3) solution at 65°C on a thermal shaker. 20 μL of 5M NaCl was added to the elute and the cross-links reversed by incubating for 6 h at 65°C. DNA was purified using Mini-elute PCR purification kit (QIAGEN).

The RARE consensus sequence was identified upstream of the Hoxa5 TSS from a previous study Mahony et al., 2011. The sequence of this region was obtained using the 'getSeq' function from the 'Biostrings' package and used to scan for the RARA::RXRA motif using the position weight matrix obtained from JASPAR2018 for vertebrates and the 'matchPWM' function from 'Biostrings'. The biggest hit was on chr6:52,134,337-52,134,389. qPCR for amplification of genomic regions of interest was described as above with the primer pairs described in the Key Resources Table.

4C template preparation

4C template was prepared as described in (van de Werken et al., 2012) with modifications. Briefly, cells were dissociated for 30 minutes at 37°C in 0.25% trypsin; 1mg/ml collagenase type II; 5mM EDTA. Cells were fixed using 2% formaldehyde/10%FCS/PBS for 10 minutes at RT. Cells were lysed for 10 minutes on ice (50mM Tris-HCl pH 7.5, 150mM NaCl, 5mM EDTA, 0.5% NP40 substitute, 1% Triton X-100, 1X proteinase inhibitors). Chromatin was digested in the context of the nucleus using the restriction enzymes NlaIII, followed by ligation. Ligated chromatin was de-crosslinked in the presence of proteinase K at 65°C O/N and subsequently treated with RNase A. Genomic DNA was extracted by beads purification and subsequently digested O/N using the restriction enzymes Csp6I and ligated under diluted conditions (16°C, O/N) favoring intra-molecular ligations. Genomic DNA was cleaned up using bead purification.

4C PCR, mapping and analysis of 4C data

The 4C PCR was performed as described in van de Werken et al., 2012, using the primers described in the Key Resources Table and sequencing was done on the Illumina HiSeq. Reads were mapped, allowing no mismatches, to a database of 4C-seq fragment-ends generated from the mm10/NCBI m38 version of the mouse genome. Interaction profiles shown are produced using all fragments (blind and non-blind) calculating a running mean with a window of 31 fragments. The profiles were normalized to the total amount of reads in *cis*.

RNA sequencing analysis

All samples were run in triplicates with three embryos per replicate. 2000 cells per sample were isolated by FACS, directly sorted into lysis buffer and snap frozen to −80°C. RNA was extracted using the PicoPure RNA Isolation Kit (Applied Biosystems) and retro-transcribed. cDNA was amplified from total RNA using the Ovation RNA Amplification System (NuGEN). Libraries were prepared using the Total RNA Sequencing TotalScript Kit (Epicenter) and sequencing was performed using Hi-Seq 2500 Illumina solid sequencer. Data analysis was performed using the Bioconductor QuasR Package (Gaidatzis et al., 2015). The cut-off for low abundant transcripts was set to 1 count per million reads in control samples. Gene Ontology analysis was performed using the GO Enrichment Analysis tool powered by PANTHER (http://geneontology.org/docs/go-enrichment-analysis/).

Virus production and tracing experiments

EnvA-Rabies-ΔG-mCherry (a kind gift of E. Callaway) or *SAD-ΔG-mCherry* viruses were produced in B19G2 and BHK-EnvA2 cells stably expressing the rabies-glycoprotein and viral titers was determined as described elsewhere (Wickersham et al., 2010). Multiple injections per animal were targeted to the cerebellar hemisphere contralateral to the electroporated PN at P2. Animals were perfused at P8. Vibratome sectioning was performed to obtain brain slices which were subsequently stained with DAPI and imaged on Zeiss Axioscan Z1, analysis was done using Fiji and IMARIS (Bitplane). For quantification of transsynaptic viral tracing experiment, we normalized the total number of transsynaptically traced *mCherry*$^+$ neurons in a given cortical area with the total number of *mCherry*$^+$ labeled cortical neurons, in order to take into consideration any variability due to electroporation or virus injection differences between distinct experiments.

AAV1.hSyn.GFP.WPRE.bGH was used for anterograde tracing from cortex. Stereotaxic injection (Kopf Instruments) was performed on isoflurane anesthetized P5 animals using picospitzer (Parker). Coordinates to target S1 cortex used bregma as a reference point for anterior-posterior (−0.58), medio-lateral (1.5-1.8) and dorso-ventral (1.0 −1.5) coordinates. Injection was targeted to the hemisphere ipsilateral to electroporated PN. Mice were perfused at P18 and dissected brains were processed for vibratome sectioning and immunohistochemistry. Only mice with confirmed anatomical precision to target region and efficient electroporation were included in further analysis.

Imaging, 3D-reconstructions and Image processing

Chromogenic staining was examined by classical wide-field or binocular microscopy (Nikon). Dual chromogenic and fluorescent imaging was done on Zeiss LSM 700 confocal microscope. Imaging of fluorescent signals was performed using an Axio imager Z2 upright microscope coupled to a LSM700 Zeiss laser scanning confocal using 5x (NA 0.25), 10x (NA 0.45), 20x (NA 0.8),40x (NA 1.3) or 63X (NA 1.4) lens.

For 3D reconstructions of the cortices, the whole brain was sliced in 50 μm sections and imaged with an Axio Scan.Z1 using a 10x (NA 0.45) lens. Different cortical regions from lateral to medial sections were mapped using imageJ ROI selector as per the mouse brain atlas (Paxinos and Franklin). Each ROI was filled in and assigned a different intensity. The resulting ROI image for each corresponding slice was saved separately. Consecutive images from medial to lateral section were aligned using TrakEM2 (incorporated into the Fiji software (http://fiji.sc)). The images with ROI were then aligned with the corresponding images. Reconstructions were visualized using Bitplane IMARIS. For 3D reconstruction of individual brain regions, the region of interest in consecutive images were cropped and saved separately. These cropped regions were aligned using TrakEM2. Reconstructions were visualized using IMARIS and the counting of neuronal cell bodies in different regions of the CNS was done with Imaris Spot detection tool.

QUANTIFICATION AND STATISTICAL ANALYSIS

Statistical details of each experiment can be found in the figure legends. Graphs were generated and statistical analysis was done with GraphPad Prism software. All results are presented as the mean + SD. Statistical significance was accepted at the $p < 0.05$ level ($p < 0.05$ = *, $p < 0.01$ = **, $p < 0.001$ = ***). Statistical significance was assessed by nonpaired, two-tailed Student's t test for the comparison of two unmatched groups, ordinary one-way ANOVA followed by Bonferroni's multiple comparisons test for more than two unmatched groups, and by ordinary two-way ANOVA followed by Bonferroni's multiple comparisons test for analysis with two factors. Comparison of RNA-seq datasets was done using Pearson correlation coefficient analysis.